

1 **Pore Water Sulfate, Alkalinity, and Carbon Isotope Profiles in Shallow**
2 **Sediment above Marine Gas Hydrate Systems: A Numerical Modeling**
3 **Perspective**

4
5
6 Sayantan Chatterjee¹, Gerald R. Dickens^{2,3}, Gaurav Bhatnagar^{1,4}, Walter G. Chapman¹,
7 Brandon Dugan³, Glen T. Snyder³ and George J. Hirasaki^{1,*}
8

9
10 A manuscript in press:

11 *Journal of Geophysical Research – Solid Earth*

12 **(DOI: 10.1029/2011JB008290)**

13 June 1, 2011

14
15 ¹Department of Chemical and Biomolecular Engineering, Rice University, Houston,
16 Texas 77005, USA

17
18 ²Department of Earth Science, Rice University, Houston, Texas 77005, USA

19
20 ³Institutionen för Geologiska Vetenskaper, Stockholms Universitet 106 91 Stockholm,
21 Sweden

22
23 ⁴Shell International Exploration and Production Inc., Houston, Texas 77082, USA
24
25

26
27 *Corresponding author:

28 Email: gjh@rice.edu (G. J. Hirasaki)

29 Phone: +1 713-348-5416

30 Fax: +1 713-348-5478

31

32 **Abstract**

33 Both the concentration and the carbon isotope composition of dissolved inorganic
34 carbon (DIC) vary considerably across the sulfate-methane transition (SMT) in shallow
35 marine sediment at locations with gas hydrate. This variability has led to different
36 interpretations for how carbon, including CH₄, cycles within gas-charged sediment
37 sequences over time. We extend a one-dimensional model for the formation of gas
38 hydrate to account for downhole changes in dissolved CH₄, SO₄²⁻, DIC, and Ca²⁺, and
39 the δ¹³C of DIC. The model includes advection, diffusion, and two reactions that
40 consume SO₄²⁻: degradation of particulate organic carbon (POC) and anaerobic
41 oxidation of methane (AOM). Using our model and site-specific parameters, steady-
42 state pore water profiles are simulated for two sites containing gas hydrate but different
43 carbon chemistry across the SMT: Site 1244 (Hydrate Ridge; DIC = 38 mM, δ¹³C of DIC
44 = -22.4‰ PDB) and Site Keathley Canyon (KC) 151-3 (Gulf of Mexico; DIC = 16 mM,
45 δ¹³C of DIC = -49.6‰ PDB). The simulated profiles for CH₄, SO₄²⁻, DIC, Ca²⁺, and δ¹³C
46 of DIC resemble those measured at the sites, and the model explains the similarities
47 and differences in pore water chemistry. At both sites, an upward flux of CH₄ consumes
48 most net SO₄²⁻ at a shallow SMT, and calcium carbonate removes a portion of DIC at
49 this horizon. However, a large flux of ¹³C-enriched HCO₃⁻ enters the SMT from depth at
50 Site 1244 but not at Site KC151-3. This leads to a high concentration of DIC with a δ¹³C
51 much greater than that of CH₄, even though AOM causes the SMT. The addition of
52 HCO₃⁻ from depth impacts the slope of certain concentration cross-plots. Crucially,
53 neither the DIC concentration nor its carbon isotopic composition at the SMT can be
54 used to discriminate between sulfate reduction pathways.

55

56 1. Introduction

57 Solid gas hydrates form when water molecules encapsulate low molecular weight
58 gas molecules at relatively high pressure, low temperature, high water activity, and high
59 gas concentration [*Sloan and Koh, 2007*]. These conditions exist along many
60 continental margins where hydrocarbon gases, usually CH₄, accumulate in sediment
61 pore space within a shallow depth interval commonly called the gas hydrate stability
62 zone (GHSZ). While their global abundance and distribution remain uncertain [*Dickens,*
63 *2001a; Milkov, 2004; Buffett and Archer, 2004; Klauda and Sandler, 2005*], marine gas
64 hydrates may constitute a future energy resource [e.g., *Collett, 2002; Walsh et al.,*
65 *2009*], a deep-water geohazard [e.g., *Borowski and Paull, 1997; Briaud and Chaouch,*
66 *1997; Kwon et al., 2010*], and an important component of the global carbon cycle [e.g.,
67 *Dickens, 2003; Archer et al., 2009*].

68 The amount and distribution of gas hydrate within the GHSZ at a given location
69 depend on *in situ* concentrations of light hydrocarbons [e.g., *Dickens et al., 1997; Xu*
70 *and Ruppel, 1999; Davie and Buffett, 2001; Milkov et al., 2003; Bhatnagar et al., 2007*].
71 In most marine settings with gas hydrate, CH₄ concentration dominates total
72 hydrocarbon concentration, and gas hydrate arises when CH₄ concentrations exceed
73 those on a dissolved gas-gas hydrate saturation curve. Usually, however, such excess
74 solubility does not occur in the upper part of the GHSZ (**Figure 1**). Instead, two
75 biogeochemical zones, separated by a thin (generally <2 m) sulfate-methane transition
76 (SMT), distinguish shallow sediment. From the seafloor to the SMT, dissolved SO₄²⁻
77 decreases from seawater concentration (~28 mM) at the seafloor to near-zero
78 concentration at the SMT; from the SMT to deeper zones, dissolved CH₄ increases from

79 near-zero concentration at the SMT to a concentration on the saturation curve below
80 **(Figure 1)**. This means that the top occurrence of gas hydrate at most locations lies
81 below the seafloor and within the GHSZ [e.g., *Dickens et al.*, 1997; *Xu and Ruppel*,
82 1999; *Davie and Buffett*, 2001; *Dickens*, 2001a; *Milkov et al.*, 2003; *Bhatnagar et al.*,
83 2007; *Malinverno et al.*, 2008]. Although a bottom simulating reflector (BSR) on seismic
84 profiles often marks the deepest presence of gas hydrate [*Kvenvolden*, 1993; *Paull and*
85 *Matsumoto*, 2000; *Tréhu et al.*, 2004], remote sensing methods face difficulties
86 detecting the shallowest gas hydrate, presumably because physical properties of
87 sediment do not change significantly when small amounts of gas hydrate are present. In
88 addition, this boundary can be hard to locate accurately in well logs and sediment cores
89 from drill holes [*Paull and Matsumoto*, 2000; *Tréhu et al.*, 2004].

90 Pore water SO_4^{2-} gradients in shallow sediment may offer a geochemical means
91 to determine underlying CH_4 gradients and the uppermost occurrence of gas hydrate.
92 Many papers have attributed SMTs in shallow marine sediment to anaerobic oxidation
93 of methane (AOM) [e.g., *Borowski et al.*, 1996, 1999; *Valentine and Reeburgh*, 2000;
94 *Dickens*, 2001b; *D'Hondt et al.*, 2004; *Snyder et al.*, 2007]. Specifically, the SMT
95 represents an interface where microbes utilize SO_4^{2-} diffusing down from the seafloor
96 and CH_4 rising up from depth according to [*Reeburgh*, 1976]:



98 This interpretation implies a 1:1 ratio of SO_4^{2-} and CH_4 fluxes into the SMT, and is
99 important to gas hydrate studies. If AOM principally causes the SMT in shallow
100 sediment above gas hydrate, and the overall system is near steady-state conditions, the

101 SO_4^{2-} gradient and the SMT depth should relate to the underlying CH_4 gradient and the
102 shallowest occurrence of gas hydrate (**Figure 1**).

103 Field observations, mass balance calculations, and numerical modeling results
104 support the assumptions and expected relationships between SO_4^{2-} and CH_4 fluxes
105 [Borowski *et al.*, 1996, 1999; Dickens, 2001b; Davie and Buffett, 2003b; Paull *et al.*,
106 2005; Snyder *et al.*, 2007; Bhatnagar *et al.*, 2008, 2011]. Nonetheless, the use of pore
107 water SO_4^{2-} profiles to constrain gas hydrate distribution remains controversial because
108 of unresolved issues. A source of current debate concerns the concentration and
109 carbon isotope composition ($\delta^{13}\text{C}$, expressed relative to Pee Dee Belemnite) of
110 dissolved inorganic carbon (DIC) at the SMT [cf. Kastner *et al.*, 2008a; Dickens and
111 Snyder, 2009]. The CH_4 in many regions with gas hydrate has a $\delta^{13}\text{C}$ of -50% or lower
112 [Milkov, 2005]. Moreover, given the ubiquitous 7.0-8.3 pH of pore water in these
113 systems [e.g., Shipboard Scientific Party, 1996, 2003a, 2003b], almost all DIC consists
114 of HCO_3^- . If AOM (**Equation 1**) primarily drives the SMT, and the systems were closed,
115 one might predict DIC at this interface to be <28 mM with a $\delta^{13}\text{C} < -50\%$ [Kastner *et al.*,
116 2008a] (the DIC being less than the loss of SO_4^{2-} because of authigenic carbonate
117 precipitation). Although this has been observed at some locations with underlying gas
118 hydrate, often DIC at the SMT is >30 mM and has a $\delta^{13}\text{C} > -30\%$ (**Figure 2**) [Paull *et al.*,
119 2000b; Borowski *et al.*, 2000; Claypool *et al.*, 2006, Torres and Rugh, 2006; Pohlman *et al.*,
120 2008; Kastner *et al.*, 2008b; Torres and Kastner, 2009; Kim *et al.*, 2011].

121 There are two basic explanations for relatively high DIC and $\delta^{13}\text{C}$ across the SMT
122 in regions with gas hydrate [cf. Kastner *et al.*, 2008a; Dickens and Snyder, 2009]. First,
123 rather than AOM, sulfate reduction of particulate organic carbon (POC) consumes much

124 of the pore water SO_4^{2-} in shallow sediment. This bacterially mediated reaction [Berner,
125 1980; Boudreau and Westrich, 1984], here and elsewhere alternatively referred to as
126 degradation of POC or organoclastic sulfate reduction, can be expressed as:



128 Notably, the reaction generates two moles of HCO_3^- for each mole of SO_4^{2-} , in contrast
129 to AOM where the stoichiometry is 1:1 (**Equation 1**). The $\delta^{13}\text{C}$ of POC in marine
130 sediments typically lies between -26‰ and -16‰ [e.g., Conrad, 2005; Kim et al., 2007],
131 and there is minimal fractionation of carbon isotopes during such sulfate reduction.
132 Sulfate consumption via POC, therefore, should lead to higher DIC concentrations with
133 greater $\delta^{13}\text{C}$ than expected from AOM [Claypool et al., 2006; Kastner et al., 2008a;
134 Torres and Kastner, 2009]. However, this explanation fails to explain the high DIC (>40
135 mM) and modest ^{13}C -depletion in DIC (<-15 ‰) at some sites (**Figure 2**). Alternatively,
136 along with CH_4 , HCO_3^- enriched in ^{13}C can enter the SMT from below. Such ^{13}C -rich
137 HCO_3^- forms during methanogenesis [e.g., Conrad, 2005], and a contribution from this
138 source would also lead to elevated DIC concentrations with relatively high $\delta^{13}\text{C}$ across
139 the SMT [Dickens and Snyder, 2009; Kim et al., 2011].

140 We assess the alternate explanations for DIC concentration and carbon isotopic
141 composition within the context of a numerical model for gas hydrate distribution. First,
142 we review two sites with gas hydrate but very different carbon chemistry across the
143 SMT. We then extend a 1-D model for gas hydrate accumulation in marine sediment
144 [Bhatnagar et al., 2007, 2008, 2011] such that it more fully incorporates carbon
145 chemistry. Specifically, we include equations for both sulfate consumption reactions
146 (**Equations 1 and 2**), coupled mass balance equations for CH_4 , SO_4^{2-} , DIC and Ca^{2+} ,

147 and coupled mass balance equations for the ^{12}C and ^{13}C of CH_4 and DIC. We show how
148 mixtures of DIC derived from AOM and from depth can explain the wide difference in
149 concentrations and $\delta^{13}\text{C}$ of DIC across the SMT at both sites, and discuss the
150 implications of this result.

151

152 **2. Pore water profiles across the sulfate-methane transition**

153 *2.1 Overview*

154 Sediment cores have been recovered from many continental margins where
155 underlying strata hosts gas hydrate [e.g., *Kvenvolden, 1993; Paull et al., 1996;*
156 *Shipboard Scientific Party, 1996, 2003a, 2003b; Snyder et al., 2007; Hiruta et al., 2009;*
157 *Kim et al., 2011*]. From these cores, pore water profiles have been generated, showing
158 how concentrations of dissolved constituents change beneath the seafloor. Not all cores
159 (or sets of cores in the case of drilling) penetrate the SMT, and very few cores have
160 been examined for a wide array of dissolved constituents at high depth resolution.
161 Nonetheless, two “end-member” cases appear to exist with regards to the concentration
162 and $\delta^{13}\text{C}$ of DIC across the SMT (**Figure 2**). These can be highlighted with data from
163 two locations, which frame current discussions regarding carbon cycling across the
164 SMT [e.g., *Claypool et al., 2006; Kastner et al., 2008a; Dickens and Snyder, 2009*], as
165 well as our modeling.

166

167 *2.2 Site 1244 (Hydrate Ridge)*

168 Ocean Drilling Program (ODP) Leg 204 drilled Site 1244 at 890m below sea level
169 (mbsl) on the eastern flank of Hydrate Ridge offshore the central coast of Oregon

170 [Tréhu *et al.*, 2003]. The pressure and temperature at the seafloor are 8.72 MPa and
171 3.8°C. Given a measured geothermal gradient of 0.061°C/m and the predominance of
172 CH₄ (>99%) in gas samples [Kvenvolden, 1995], the base of the GHSZ should be ~133
173 m below seafloor (mbsf). Seismic data indicate a BSR at ~124 mbsf [Tréhu *et al.*, 2003].
174 As true with many locations, however, the amount and distribution of gas hydrates
175 between the seafloor and the base of the GHSZ remain uncertain. Various approaches
176 for detecting and quantifying gas hydrate suggest average gas hydrate saturation
177 between 2 and 10% of pore space below a depth at around 50 mbsf, which is
178 apparently the top of the gas hydrate zone [Tréhu *et al.*, 2003; Lee and Collett, 2006].

179 Headspace CH₄ concentrations rise from 0.2 to 6.5 mM between 7 and 16 mbsf
180 [Shipboard Scientific Party, 2003b]. Beyond this depth, *in situ* methane concentrations
181 exceed those for gas solubility after core recovery (~STP), so they have little meaning
182 [Paull *et al.*, 2000a; Shipboard Scientific Party, 2003b]. Methane δ¹³C values range
183 between -65‰ and -77‰ [Milkov *et al.*, 2005; Claypool *et al.*, 2006]. The amount and
184 average isotopic composition of organic carbon through the sequence are 1.27 wt%
185 [Shipboard Scientific Party, 2003b] and -24‰ [Yu *et al.*, 2006], respectively.

186 The SO₄²⁻ profile at Site 1244 (**Figure 3a**; [Tréhu *et al.*, 2003]) is somewhat
187 complicated. Values decrease from 29.7 mM near the seafloor to 21.3 mM at ~4 mbsf;
188 below, they drop nearly linearly to <1 mM by 9.2 mbsf. This is where CH₄ rises above
189 1.8 mM, and dissolved Ba²⁺ increases markedly [Tréhu *et al.*, 2003]. The latter is
190 noteworthy because Ba²⁺ profiles (when measured) often show a steep rise just below
191 the SMT [e.g., Snyder *et al.*, 2007].

192 Alkalinity increases from 2.8 mM near the seafloor to 37 mM at 8.5 mbsf; below,
193 it rises to ~64 mM at 37 mbsf (**Figure 3b**; [Tréhu *et al.*, 2003]). The pH throughout the
194 interval is between 7.1 and 8.1 [*Shipboard Scientific Party*, 2003b], strongly suggesting
195 that alkalinity, DIC and HCO_3^- concentrations are nearly the same. Thus, there is a
196 distinct change in HCO_3^- gradients across SMT, but values continue to rise with depth.

197 Dissolved Ca^{2+} is ~10 mM near the seafloor and decreases to ~4 mM at the
198 SMT; below, it slowly decreases (**Figure 3c**; [Tréhu *et al.*, 2003]). An obvious inflection
199 in Ca^{2+} concentrations, opposite to that of alkalinity, spans the SMT.

200 Profiles of DIC $\delta^{13}\text{C}$ also display inflections across the SMT. The $\delta^{13}\text{C}$ of DIC is
201 0‰ near the sediment-water interface and decreases to a minimum of -22.5‰ at ~7.8
202 mbsf. Values then increase to +15‰ by ~55 mbsf (**Figure 3d**; [Torres and Rugh,
203 2006]). Importantly, the $\delta^{13}\text{C}$ profile displays “concave-down” curvature below the SMT.

204

205 2.3 Site KC151-3 (Keathley Canyon)

206 A Department of Energy-sponsored Joint Industry Program drilled Site KC151-3
207 at 1322 mbsl in Keathley Canyon in the northern Gulf of Mexico [Ruppel *et al.*, 2008].
208 The pressure and temperature at the seafloor are 12.95 MPa and 4°C. Given the
209 geothermal gradient of 0.038°C/m and the predominance of CH_4 in gas samples, the
210 base of the GHSZ should be at ~314 mbsf. A BSR is present between ~380 mbsf
211 [Kastner *et al.*, 2008b] and 390 mbsf [Ruppel *et al.*, 2008]. Several studies showed
212 uneven distribution of gas hydrates in fractured silty-clayey sediments between 220 and
213 300 mbsf occupying 1-12% of pore volume [e.g., Cook *et al.*, 2008; Lee and Collett,
214 2008; Kastner *et al.*, 2008b]. Cook *et al.* [2008] reported a few occurrences of fracture-

215 filled hydrates in the shallow sandy clays between 110 and 115 mbsf, which might be
216 interpreted as being near the top of the gas hydrate zone.

217 Headspace CH₄ concentrations rise from 0 to 13.8 mM between 5 and 12 mbsf
218 [Lorenson *et al.*, 2008]. Again, deeper values probably represent residual CH₄ after
219 significant degassing [Paull *et al.*, 2000a; Lorenson *et al.*, 2008]. Methane δ¹³C values
220 increase from -78.2‰ to -73.8‰ between 16 and 44 mbsf, and remain ~-72‰ in deeper
221 strata [Lorenson *et al.*, 2008]. The amount of organic matter in the sediment sequence
222 ranges from 0.44% to 0.95% [Winters *et al.*, 2008]. The δ¹³C of bulk sediment organic
223 matter ranges from -19.7‰ to -21.7‰ in this region, at least near the sediment-water
224 interface [Goni *et al.*, 1998].

225 The SO₄²⁻ concentration profile at Site KC151-3 (**Figure 3a**; [Kastner *et al.*,
226 2008b]) has a profile somewhat similar to that at Site 1244. Values decrease from ~28
227 mM near the seafloor to 16.5 mM at ~7 mbsf; below, they drop to <1 mM at ~10.4 mbsf.

228 By contrast, the alkalinity profile (**Figure 3b**; [Kastner *et al.*, 2008b]) is much
229 different than that at Site 1244. Alkalinity gradually increases from <3 to 6.7 mM across
230 the upper 6 m of sediment, and reaches a maximum of 16.1 mM at 10.4 mbsf. Alkalinity
231 then drops, such that it is <4 mM at 24 mbsf. Assuming that alkalinity comprises mostly
232 HCO₃⁻, there is an obvious bicarbonate peak at the SMT.

233 Dissolved Ca²⁺ is ~10 mM near the seafloor and decreases to ~8 mM at the
234 SMT; below, it slowly increases to ~14 mM at greater depths of ~40 mbsf (**Figure 3c**;
235 [Kastner *et al.*, 2008b]). Thus, as at Site 1244, there is a minimum in Ca²⁺ at the SMT.
236 However, the Ca²⁺ profile is complicated at Site KC151-3 because a brine exists at
237 depth [Kastner *et al.*, 2008b]. Extremely saline water with high concentrations of Ca²⁺

238 (and other species) fills pore space of deep sediment across much of the northern Gulf
239 of Mexico [e.g., *Kharaka et al.*, 1987; *Macpherson*, 1989; *Castellini et al.*, 2006].

240 As at Site 1244, the $\delta^{13}\text{C}$ of DIC has a minimum at the depth of maximum
241 alkalinity (**Figure 3d**; [*Kastner et al.*, 2008b]). However, it drops from 0‰ near the
242 seafloor to -49.6‰ at this horizon, and increases to only +6‰ by 100 mbsf. Thus, the
243 $\delta^{13}\text{C}$ of DIC exhibits a clear inflection across the SMT, but is generally lower beneath
244 the SMT compared to Site 1244.

245

246 **3. Numerical model**

247 *3.1 General framework*

248 Several one-dimensional (1-D) numerical models for gas hydrate accumulation in
249 marine sediment have been developed [e.g., *Rempel and Buffett*, 1997; *Egeberg and*
250 *Dickens*, 1999; *Xu and Ruppel*, 1999; *Davie and Buffett*, 2001, 2003a, 2003b; *Liu and*
251 *Flemings*, 2007; *Bhatnagar et al.*, 2007]. Although they have notable differences, these
252 models have similar conceptual frameworks. A series of coupled mathematical
253 expressions (i.e., mass, momentum and energy transport equations) express the
254 following basic processes. Particles, including organic carbon, settle on the seafloor and
255 become part of sediment, which has seawater within pore space. During burial,
256 pressure and temperature increase, porosity decreases, and a fraction of POC converts
257 to CH_4 below the SMT. Methane can also be contributed from depth. Dissolved CH_4 can
258 move between sediment depths during burial because of diffusion, advection, or both.
259 At appropriate pressure, temperature and water activity, dissolved CH_4 concentrations
260 can surpass those for gas hydrate or free gas saturation. Eventually, steady-state

261 conditions are reached. At this point, as well as at transient states before, there is a
262 distribution of CH₄ with respect to depth. The CH₄ can occur dissolved in water, as gas
263 hydrate, or within free gas.

264 There are problems with current 1-D models. In particular, they do not account
265 for changes in water activity (~salinity) caused by gas hydrate formation and
266 dissociation [e.g., *Egeberg and Dickens*, 1999; *Milkov et al.*, 2004], for heterogeneities
267 in sediment properties over depth [e.g., *Tréhu et al.*, 2003; *Malinverno et al.*, 2008], or
268 for lateral variations in various parameters. As such, resulting simulations give broad
269 profiles for the amount of CH₄ occurring dissolved in water, in gas hydrate, and in free
270 gas with respect to depth. The various models also include several assumptions. For
271 example, reaction rates and diffusion coefficients do not change with depth and
272 temperature in the model by *Bhatnagar et al.* [2007]. Nonetheless, when appropriate
273 parameters are incorporated, the CH₄ profiles generated from numerical modeling
274 provide good first-order descriptions of CH₄ profiles at sites that have been examined by
275 direct measurements [e.g., *Davie and Buffett*, 2001, 2003a; *Liu and Flemings*, 2007;
276 *Bhatnagar et al.*, 2007, 2011].

277

278 3.2 Basic model

279 One recent and encompassing 1-D numerical model for gas hydrate
280 accumulation in marine sediments has been developed and described by *Bhatnagar et*
281 *al.* [2007]. This model differs from others in two important aspects. First, it computes
282 mass balances for a system in thermodynamic equilibrium over geologic timescales, so
283 avoids the necessity of kinetics regarding hydrate formation. Second, it frames results in

284 terms of dimensionless groups. This enables identification of key factors controlling gas
285 hydrate distribution and accumulation, and allows results to be compiled (and
286 compared) for a wide range of model parameters.

287 Three sets of mathematical expressions underpin this model [*Bhatnagar et al.*,
288 2007]. There are those that: (1) calculate appropriate CH₄ phase equilibrium and
289 solubility curves; (2) describe sediment burial and porosity reduction; and (3) account
290 for mass conservation of CH₄, water, and organic carbon. The latter includes
291 expressions for CH₄ diffusion driven by concentration gradients, fluid advection resulting
292 from sediment burial and compaction, and external fluid flow caused by overpressure in
293 deeper sediments. Parameters and equations for this model are presented, defined and
294 explained by *Bhatnagar et al.* [2007]. We re-introduce some of these here for
295 clarification and expansion.

296 In the original model, CH₄ escaped the GHSZ over time through burial (as
297 dissolved gas or free gas) or through the seafloor. Clearly, the latter does not happen at
298 most locations, because of an SMT at or near the seafloor (**Figure 1**). The model was
299 thus extended with mathematical expressions that coupled CH₄ and SO₄²⁻ consumption
300 in shallow sediment [*Bhatnagar et al.*, 2008, 2011]. It was assumed that CH₄ drove all
301 *net* SO₄²⁻ consumption, following arguments made by numerous authors [e.g.,
302 *Reeburgh*, 1976; *Borowski et al.*, 1996, 1999; *Snyder et al.*, 2007]. Both the original and
303 revised models give good first-order estimates for the amount and distribution of gas
304 hydrate at different sites (e.g., ODP Sites 889 and 997; IODP Sites U1325 and U1326)
305 with appropriate input parameters [*Bhatnagar et al.*, 2007, 2008, 2011]. However, the
306 models were not evaluated with coupled mass balances for carbon. Other models for

307 gas hydrate accumulation likewise do not track DIC, its carbon isotope composition, and
 308 authigenic carbonate precipitation. Without revision, they cannot be used to assess the
 309 divergent explanations for the concentration and $\delta^{13}\text{C}$ of pore water DIC across the
 310 SMT.

311

312 *3.3 Updated model: Reactions*

313 Carbon cycling within and above marine gas hydrate systems involves multiple
 314 chemical reactions. At the most basic level, four must be considered (excluding those
 315 relating to CH_4 phase changes). These are, with their corresponding rates:

316 (i) Methanogenesis (fermentation in sediment below the SMT)



318 (ii) Anaerobic oxidation of methane (at the SMT)



320 (iii) Organoclastic sulfate consumption (between the seafloor and the SMT)



322 (iv) Authigenic carbonate (calcite) precipitation (below the seafloor)



324 where r = rate of reaction, λ = first-order methanogenesis reaction rate constant, λ_{AOM}
 325 and λ_{POC} refer to second-order reaction rate constants for AOM and POC-driven sulfate
 326 consumption respectively; α = organic carbon content in sediment, c = component
 327 mass fraction, and t = time; and, the subscripts m , s , CaCO_3 refer to CH_4 , SO_4^{2-} , and
 328 CaCO_3 components respectively, and the superscript l refers to the liquid phase

329 (**Appendix A**). Note that the first three reactions (**Equations 3-5**) are modeled as
330 irreversible and expressed with a kinetic rate, while the fourth reaction (**Equation 6**) is
331 modeled as a reversible equilibrium reaction. Whenever pore water concentrations
332 exceed equilibrium, we assume stoichiometric amounts of DIC and Ca^{2+} precipitate as
333 calcium carbonate. The rate of this reaction in the model is the amount of calcium
334 carbonate formed over a unit timestep. Thus, our model ignores hydrate formation
335 kinetics but includes CH_4 formation kinetics (**Equation 3**).

336 We acknowledge that methanogenesis (**Equation 3**) involves intermediate
337 reactions (**Appendix B**). We also assume that excess H^+ produced by the above
338 reactions forms dissolved organic acids and ammonium ion, because pore waters in
339 gas hydrate systems can have a deep yellow color and very high NH_4^+ concentrations
340 [e.g., *Shipboard Scientific Party*, 1996, 2003a, 2003b]. These species can then advect
341 or diffuse, although we do not model this. Lastly, we equate carbonate precipitation to
342 calcite precipitation throughout this work for simplicity. Authigenic calcite certainly forms
343 near the SMT above many gas hydrate systems [e.g., *Rodriguez et al.*, 2000; *Snyder et*
344 *al.*, 2007], although other carbonate minerals (aragonite and dolomite) can also
345 precipitate [*Bohrmann et al.*, 1998; *Greinert et al.*, 2001].

346

347 *3.4 Updated model: Equations*

348 Starting with the existing model framework [*Bhatnagar et al.*, 2007, 2008], key
349 mass balance equations are revised (**Appendix C**) to include organoclastic sulfate
350 consumption (**Equation 5**) and calcite precipitation (**Equation 6**). Additionally, we track
351 the ^{12}C and ^{13}C isotope compositions of CH_4 and DIC, the two carbon species in our

352 model. We determine ^{12}C and ^{13}C compositions of CH_4 and DIC by multiplying the
353 concentration and $^{13}\text{C}/^{12}\text{C}$ ratio of the species. Isotope compositions are then
354 normalized to those of the Pee Dee Belemnite (PDB) standard, such that they are
355 computed and expressed in conventional delta notation ($\delta^{13}\text{C}$) over time and depth.

356 The mass balance equations are then rewritten in dimensionless form (**Appendix**
357 **C**) following previous work [*Bhatnagar et al.*, 2007, 2008, 2011]. This reduces the
358 number of parameters describing a particular system, and allows for straightforward
359 comparisons of different systems from a mechanistic perspective.

360

361 *3.5 Numerical solution*

362 The dimensionless mass balance equations (**Equations C23-C29**) were solved
363 in conservative form for specified initial and boundary conditions (**Equations C32-C46**)
364 to obtain steady-state solutions. The hyperbolic dimensionless partial differential
365 equation for POC (**Equation C23**) was solved numerically using an implicit, block-
366 centered, finite-difference scheme. To solve the other six equations (**Equations C24-**
367 **C29**), explicit numerical schemes were formulated. These six partial differential
368 equations were recast in a finite difference form and solved with simultaneous update of
369 the POC profile in time. Solution to the above equations ensured no material loss (all
370 simulations had material balance errors $<10^{-8}$). A single-point, upstream weighting was
371 used to formulate the sediment and fluid advection terms. To calculate fluxes across
372 numerical grid faces, upstream grid point values (for species concentration) were used,
373 as opposed to using average values at two adjacent grid points.

374

375 4. Results and Discussion

376 4.1 Steady state concentration profiles

377 4.1.1 Case 1: Site 1244

378 Site 1244 is characterized by significant CH₄ generation at relatively shallow
379 depth ($z < L_t$), and relatively low fluid advection [Pohlman et al., 2009]. Steady-state
380 concentration profiles were simulated (**Figure 4**) for parameters (**Table 1**) given or
381 inferred from reports for this location [Tréhu et al., 2003]. The sedimentation rate was
382 used to calculate a Pe_1 of 0.044. Because this relates to sediment burial and porosity
383 reduction (**Equation C18**), this parameter was fixed for all simulations at this location.

384 The thickness of the SMT (as opposed to depth) should depend on Da_{AOM}
385 [Bhatnagar et al., 2008]. The dimensionless number, Da_{AOM} characterizes the rate of
386 AOM reaction to diffusion. We chose $Da_{AOM} = 10^8$ for all simulations unless otherwise
387 specified, because this results in a thin overlap of CH₄ and SO₄²⁻ profiles at the SMT, as
388 observed in many locations (although difficult to prove at Site 1244 with the low sample
389 resolution, **Figure 3a**).

390 The normalized dissolved CH₄ concentration profile (**Figure 4a**) shows near-zero
391 values at the SMT ($\tilde{z} = 0.08$ or 10.6 mbsf) underlain by a rapid rise with increasing depth
392 (*n.b.*, concentration profiles are plotted to the base of the GHSZ, $\tilde{z} = 1$, although
393 simulated to $\tilde{z} = 2$). Upon exceeding local solubility conditions, excess CH₄ would form
394 gas hydrate. This depth occurs at $\tilde{z} = 0.65$ (or 86 mbsf), with the chosen parameters
395 (**Table 1**) and $Pe_2 = -1$, which relates to an upward fluid velocity 0.2 mm/yr. There
396 should exist relationships between pore water SO₄²⁻ concentrations, pore water CH₄

397 concentrations, CH₄ solubility, and the shallowest occurrence of gas hydrate (**Figure 1**).
398 These are emphasized elsewhere [Bhatnagar et al., 2008, 2011]. Here, the primary
399 points are that CH₄ rises from depth due to a combination of advection and diffusion,
400 and it decreases to near zero concentration at the SMT. The overall profile emerges
401 because of dissolved CH₄ production below the SMT, because of internal cycling of
402 methane phases within the GHSZ (although not specifically modeled in this paper), and
403 because of AOM at the SMT. Moreover, as discussed below, an increase in upward
404 fluid flux moves the methane profile and the SMT to shallower depths.

405 Normalized SO₄²⁻ concentrations drop nearly linearly from unity at the seafloor to
406 effectively zero at the SMT (**Figure 4a**). This depth lies at $\tilde{z} = 0.08$ (10.6 mbsf) with the
407 aforementioned initial estimates, and relatively high and low values for dimensionless
408 groups related to rates for AOM ($Da_{AOM} = 10^8$) and organoclastic sulfate reduction
409 ($Da_{POC} = 10^0$). The combination of AOM (at the SMT) and organoclastic sulfate reduction
410 (between the seafloor and the SMT) removes all SO₄²⁻. However, with these group
411 values, AOM dominates *net* SO₄²⁻ consumption.

412 The depth of the SMT should change with upward methane flux [e.g., Borowski
413 et al., 1996; Davie and Buffett, 2003b; Bhatnagar et al., 2008]. This can be simulated
414 under conditions of finite Pe_1 but varying Pe_2 (**Figure 4**). For example, with conditions
415 stated so far, as the magnitude of Pe_2 rises from 1 to 3, the SMT shoals from $\tilde{z} = 0.08$ to
416 $\tilde{z} = 0.03$ (4 mbsf). The SO₄²⁻ profile at Site 1244 exhibits a slight concave-up curvature
417 above the SMT, which could reflect a drop in sediment porosity with increasing depth
418 over the upper few meters [Dickens, 2001b]. Physical property records at Site 1244

419 appear consistent with this interpretation [*Shipboard Scientific Party*, 2003b], although
420 we have not incorporated such heterogeneity into our simulations.

421 The case where Pe_2 is -1 is particularly interesting. This gives pore water CH_4
422 and SO_4^{2-} profiles similar to those at Site 1244, including an SMT at 10.6 mbsf ($\tilde{z} = 0.08$)
423 (**Figure 4a**). Moreover, with $Pe_2 = -1$, the CH_4 profile intersects the solubility curve at
424 $\tilde{z} = 0.65$ (86 mbsf), (not shown here). This would mark the shallowest occurrence of gas
425 hydrate, which is about the depth (50 mbsf) reported in field observations [*Tréhu et al.*,
426 2003; *Lee and Collett*, 2006].

427 With the initial estimate ($Pe_2 = -1$), the model simultaneously simulates
428 normalized pore water profiles of DIC and Ca^{2+} concentrations, and the $\delta^{13}C$ of DIC. For
429 DIC, values increase from unity at the seafloor ($c_{b,o} = 2.4$ mM) to 16.6 (= 39.8 mM) at the
430 SMT ($\tilde{z} = 0.08$); below, values increase more gradually with depth, giving rise to a
431 curvature similar to observations (**Figure 4b**). The overall shape arises for three primary
432 reasons: first, methanogenesis generates considerable DIC at depth; second, this DIC
433 enters the SMT through advection and diffusion to mix with DIC generated by AOM;
434 third, DIC decreases from the SMT to the seafloor as it leaves the sediment through
435 advection and diffusion. Calcite precipitation also removes a small amount of DIC within
436 0.5 m around the SMT.

437 The previously-noted simulations with different Pe_2 demonstrate the effect of
438 increasing upward fluid flux upon the shape of the DIC profile (**Figure 4b**). As external
439 advection (and CH_4 input from depth) increases, the SMT shallows and the production
440 of DIC at this horizon (by AOM) accelerates. In addition, greater amounts of DIC
441 generated by methanogenesis ascend with pore fluids. The total effect is to amplify the

442 “kink” in the DIC profile, such that greater amounts of DIC leave the system through the
443 seafloor.

444 Normalized Ca^{2+} concentrations (**Figure 4c**) decrease from unity at the
445 sediment-water interface ($c_{\text{Ca},o} = 10 \text{ mM}$) to 0.37 (= 3.7 mM) at the SMT. Below this,
446 values continue to drop, although at a more gradual rate. The generic shape of the Ca^{2+}
447 profile arises for three fundamental reasons: first, seawater Ca^{2+} enters the SMT from
448 above, through diffusion; second, advection carries the fluid upward ($Pe_1 + Pe_2 < 0$); and
449 third, Ca^{2+} reacts with DIC to precipitate as carbonate. These factors also make the
450 Ca^{2+} concentration profile a “mirror-image” of the DIC profile (albeit somewhat
451 distorted). As such, an increase in upward fluid flux changes the shape of the Ca^{2+}
452 profile predictably: above the SMT, the gradient steepens; below the SMT, the gradient
453 lessens slightly (**Figure 4c**). This is because fluids depleted in Ca^{2+} rise from depth and
454 increased fluid flux causes greater CaCO_3 precipitation. Additionally, increased delivery
455 of DIC from below promotes CaCO_3 precipitation and likewise the demand for Ca^{2+} from
456 seawater, resulting in the steepened Ca^{2+} gradients above the SMT.

457 The steady state profile for the $\delta^{13}\text{C}$ of DIC (**Figure 4d**) is especially interesting.
458 For the initial estimates, the $\delta^{13}\text{C}$ of DIC drops from zero at the seafloor to -26‰ at the
459 SMT, but with “concave-down” curvature; below the SMT, it increases with depth to
460 more positive values (+20‰), again with “concave-down” curvature. Importantly, the
461 value at the SMT and the shape around the SMT are not prescribed in the model.
462 Instead, these occur for two reasons. First, DIC produced during methanogenesis and
463 having an initial $\delta^{13}\text{C}$ of +20‰ rises from depth to mix with DIC generated at the SMT
464 and having a $\delta^{13}\text{C}$ of -66‰. Second, this “mixed-source” DIC moves toward the

465 seafloor, where DIC is fixed at 0‰. With an increase in external fluid flux, the $\delta^{13}\text{C}$ of
466 DIC at the SMT attains a negative peak ($\sim -25\text{‰}$ when $Pe_2 = -3$) at a relatively shallower
467 depth. In summary, this pore water $\delta^{13}\text{C}$ profile arises in a system where AOM
468 dominates *net* consumption of SO_4^{2-} in shallow sediment.

469

470 4.1.2 Case 2: Site KC151-3

471 Site KC151-3 differs from Site 1244 in two fundamental ways: fluids rich in CH_4
472 and poor in SO_4^{2-} rise from depth but at a relatively high rate [*Dugan, 2008; Daigle and*
473 *Dugan, 2010*]; and concentrations of pore water DIC and Ca^{2+} are low (<10 mM) and
474 high (>20 mM), respectively, at the base of the simulated domain. We model pore water
475 concentration profiles at Site KC151-3 (**Figure 5**) in an identical manner to those at Site
476 1244, but with a different set of parameters based on observations for Site KC151-3
477 (**Table 1**).

478 From the sedimentation rate, we calculated a Pe_1 of 0.095. Our initial estimate for
479 Pe_2 was -2, which relates to an upward fluid velocity 0.17 mm/yr (comparable to $Pe_2 = -$
480 1 at Site 1244). The dimensionless groups related to AOM rate ($Da_{AOM} = 10^8$) and
481 organoclastic sulfate reduction ($Da_{POC} = 10^0$) used to model location KC151-3 were the
482 same as used for Site 1244. The combined effects of AOM (at the SMT) and
483 organoclastic sulfate reduction (between the seafloor and the SMT) are responsible for
484 *net* SO_4^{2-} consumption, although owing to the relatively low value of Da_{POC} , AOM is
485 dominant also at KC151-3.

486 The normalized dissolved CH₄ profile (**Figure 5a**) is zero between the seafloor
487 and the SMT ($\tilde{z}=0.05$ or 15.7 mbsf). Below 15.7 mbsf, it shows a rapid increase with
488 depth. Methane concentrations intersect those on the solubility curve at $\tilde{z}=0.45$ (or 141
489 mbsf). This should mark the shallowest possible occurrence of gas hydrate, but log
490 interpretations suggest gas hydrate occurs between 110 and 115 mbsf [Cook *et al.*,
491 2008].

492 Normalized, steady-state SO₄²⁻ concentrations (**Figure 5a**) decrease nearly
493 linearly from unity at the sediment-water interface to near-zero at the SMT ($\tilde{z}=0.05$). As
494 at Site 1244, the SO₄²⁻ data exhibit a slight concave-up curvature above the SMT at Site
495 KC151-3. The simulated SO₄²⁻ profile does not show such curvature, and this may again
496 relate to a drop in porosity over the first few meters.

497 Upon increasing the external fluid flux (and the magnitude of Pe_2), the SMT
498 shoals (**Figure 5a**). For one particular parameter choice ($Pe_2 = -3$), the SO₄²⁻ profile
499 drops to near-zero concentration at $\tilde{z}=0.031$. This implies that the SMT and the top of
500 gas hydrate occur at ~9.8 mbsf and ~82 mbsf ($\tilde{z}=0.26$), respectively. These values
501 agree favorably with field data, which suggest 10.4 mbsf and 110 mbsf respectively.

502 Normalized DIC profiles (**Figure 5b**) contrast markedly with those at Site 1244,
503 irrespective of fluid flux. For the initial estimate, concentrations increase with depth until
504 the SMT, below which they decrease to very low values (~4 mM). The prominent DIC
505 peak at the SMT arises for four primary reasons: first, and most importantly, AOM
506 generates DIC at the SMT; second, this DIC, through advection and diffusion, leaves
507 the SMT; third, methanogenesis produces DIC at depth; fourth, pore fluids enriched in

508 Ca^{2+} react with DIC below the SMT. Calcite precipitation also removes relatively more
509 DIC below the SMT at this location.

510 An increase in upward fluid flux changes the shape of the DIC profile above and
511 below the SMT (**Figure 5b**). However, the reason is somewhat different than that for
512 Site 1244. A higher fluid flux results in greater CH_4 input to the SMT, greater DIC
513 generation by AOM, greater DIC input to the SMT from depth, and greater DIC removal
514 from the SMT towards the seafloor. It also raises the Ca^{2+} input from depth, which leads
515 to greater calcite precipitation, below the SMT. Similar to SO_4^{2-} , DIC profiles also
516 approach the field data for a value of $Pe_2 = -3$.

517 Normalized pore water Ca^{2+} concentrations (**Figure 5c**) drop from unity at the
518 seafloor to a low value at the SMT and then increase to a constant value at depth. The
519 shape of Ca^{2+} profiles arises for multiple reasons: first, Ca^{2+} from the ocean water
520 enters the SMT from above due to diffusion; second, a high flux of Ca^{2+} enters the SMT
521 from deeper strata, through advection and diffusion; a third, significant amount of calcite
522 precipitates. The combination gives rise to the unusual Ca^{2+} profile with a “dip” below
523 the SMT. A higher upward fluid flux compresses this dip because of greater Ca^{2+} input
524 from depth, and because of greater calcite precipitation (**Figure 5c**). Our model
525 matches the data well when $Pe_2 = -3$.

526 The modeled profiles of DIC $\delta^{13}\text{C}$ differ significantly from those at Site 1244 in
527 terms of magnitude (**Figure 5d**). For the initial estimate ($Pe_2 = -2$), normalized $\delta^{13}\text{C}$ of
528 DIC is zero at the seafloor, drops to an extreme of -62‰ at the SMT, and then
529 increases gradually with depth, but only to 10‰ . On increasing fluid flux from depth, the

530 $\delta^{13}\text{C}$ values similarly drops from 0‰ to a negative peak at a relatively shallower SMT,
531 then increases more rapidly to more positive values at greater depth.

532 Crucially, the values and the curvature of the DIC $\delta^{13}\text{C}$ profile result from
533 modeling the CH_4 and SO_4^{2-} mass balances using basic parameters for the site; they
534 are not specified. Moreover, and importantly, the values and the curvature arise for
535 same general reasons as at Site 1244. The difference between the sites mainly occurs
536 because the flux and carbon isotopic composition of DIC entering the SMT from below
537 are less at KC151-3, and because the DIC produced at SMT (by AOM) has a more ^{13}C -
538 depleted value ($\delta^{13}\text{C} = -70\text{‰}$). In other words, the proportion of DIC entering the SMT
539 from depth versus that produced by AOM is much lower at Site KC151-3 compared to
540 Site 1244. This gives a lower DIC concentration at the SMT and a more negative peak
541 in DIC $\delta^{13}\text{C}$ at the SMT.

542

543 *4.2 Variations in AOM and Organoclastic Sulfate Reduction*

544 Anaerobic oxidation of methane at the SMT with minimal organoclastic sulfate
545 reduction at or above this horizon explains pore water profiles across the SMT at Sites
546 1244 and KC151-3. The very different carbon chemistry at these sites is predicted by
547 the numerical simulations because of major differences in the supply and isotope
548 composition of DIC from depth. So far, an unresolved issue is how changes in the
549 relative proportion of AOM and organoclastic sulfate reduction would affect the profiles.
550 This can be assessed by changing Da_{AOM} and Da_{POC} in model simulations for Site 1244.

551 A decrease in Da_{AOM} from its initial value of 10^8 to 10^5 illustrates the effect of this
552 dimensionless number on pore water profiles (**Figure 6a**) with same parameters used to

553 simulate the field data at Site 1244 (**Appendix A**). As reported by *Bhatnagar et al.*
554 [2008], a decrease in Da_{AOM} slows the AOM reaction, and leads to a thicker SMT.
555 Because the SMT horizon is usually thin (<2 m), this small value of Da_{AOM} is probably
556 unrealistic. Moreover, a smaller Da_{AOM} lowers the DIC generation at the SMT by AOM,
557 and the Ca^{2+} removal by calcite formation. This would render higher Ca^{2+}
558 concentrations at and above the SMT, and a more negative $\delta^{13}C$ values for DIC. These
559 simulated profiles ($Da_{AOM} = 10^5$) would not match data at the site, suggesting typical
560 values of Da_{AOM} are slightly on the high side. Thus, it is unlikely to have a small Da_{AOM} ,
561 implying relatively greater proportion of AOM reaction at the SMT at Site 1244.

562 An increase in Da_{POC} should result in higher consumption of POC and SO_4^{2-}
563 between the seafloor and the SMT, resulting in higher DIC generation above the SMT.
564 This would deplete SO_4^{2-} at a faster rate and result in non-linear profiles with a
565 “concave-down” curvature. The pore water SO_4^{2-} profile is near-linear above the SMT at
566 most locations overlying gas hydrate. Thus, increasing Da_{POC} does not result in non-
567 linear profiles if AOM is dominated ($Da_{AOM} = 10^8$). Consequently, POC also gets
568 depleted faster, leading to less available POC to form CH_4 , thereby reducing the
569 production of CH_4 and DIC by methanogenesis. As a result, the fluids are richer in Ca^{2+}
570 and $\delta^{13}C$ of DIC is much more negative due to low DIC flux entering the SMT from
571 below (**Figure 6b**). Hence, increased $Da_{POC} (=10^5)$ is not realistic, since we cannot
572 match the data and non-linear (“concave-down” curvature) SO_4^{2-} profiles are not
573 commonly observed at most sites. Furthermore, AOM, is always more dominant over
574 organoclastic sulfate reduction and influences shape of profiles across the SMT.

575

576 4.3 Concentration Cross-plots of Alkalinity and Sulfate

577 Excess alkalinity (Alk*) represents the amount of DIC that would occur in pore
578 water if authigenic carbonate had not precipitated; it can be calculated by summing the
579 deviations in pore water alkalinity, Ca^{2+} , and Mg^{2+} relative to their respective
580 concentrations in seawater. Plots can be constructed showing changes in excess
581 alkalinity (ΔAlk^*) versus changes in SO_4^{2-} (ΔSO_4^{2-}) (**Figure 7**). Such cross-plots have
582 been used to interpret the relative influence of organoclastic sulfate reduction and AOM
583 upon SO_4^{2-} consumption in sediment above the SMT [e.g., *Claypool et al.*, 2006;
584 *Kastner et al.*, 2008a; *Torres and Kastner*, 2009]. Because of the different molar
585 quantities in the reactions (**Equations 1 and 2**), the idea has been that a, 1:1 slope
586 would support SO_4^{2-} removal by AOM, a 2:1 slope would support SO_4^{2-} removal by
587 POC, and a slope in between would support consumption by both processes. Data from
588 Site KC151-3 above the SMT lie on a 1:1 slope (**Figure 7**). By contrast, at Site 1244, a
589 nearly 2:1 slope in $\Delta\text{Alk}^* : \Delta\text{SO}_4^{2-}$ characterizes pore waters above the SMT (**Figure 7**).
590 This observation has been argued to indicate POC driven SO_4^{2-} consumption at Site
591 1244 [*Kastner et al.*, 2008a], However, presentation and discussion of the data in such
592 a manner assumes a closed system with little or no mass transfer of dissolved
593 constituents, and fails to account for changes in DIC below the SMT [*Dickens and*
594 *Snyder*, 2009].

595 The departure of alkalinity (DIC) and SO_4^{2-} concentrations relative to their
596 respective seawater values can be obtained from the simulated steady-state pore water

597 profiles. Because we have not included Mg^{2+} in our modeling, ΔAlk^* is only computed
598 using DIC and Ca^{2+} concentrations. We consider a series of simulations.

599 For the first three simulations, parameters pertain to Site 1244. However, the
600 fluid flux and the relative proportion of SO_4^{2-} consumption by AOM and organoclastic
601 sulfate reduction are adjusted by changing Pe_2 , Da_{AOM} and Da_{POC} (**Figure 8**). All three
602 simulations give a 2:1 relation in $\Delta Alk^*:\Delta SO_4^{2-}$ (**Figure 8**).

603 In the first case, there is zero external fluid flux, no methanogenesis, no AOM
604 and only organoclastic sulfate reduction. Although a 2:1 slope in $\Delta Alk^*:\Delta SO_4^{2-}$ occurs,
605 pore water profiles (not shown here) do not conform to observations. Pore water SO_4^{2-}
606 decreases gradually with a “concave-down” curvature. Pore water DIC increases with
607 depth until the SMT, below which it attains a constant value as DIC is carried down by
608 advection (burial) and diffusion. The $\delta^{13}C$ of DIC is zero at the seafloor, and attains a
609 constant negative value at and below the SMT. Without methanogenesis, there is no
610 change in the DIC and $\delta^{13}C$ of DIC below the SMT.

611 In the second and the third cases, there is a low fluid flux ($Pe_2 = -0.1$),
612 methanogenesis (and thus a deep source of DIC), and AOM. The third case includes
613 organoclastic sulfate reduction. In these cases, a 2:1 slope in $\Delta Alk^*:\Delta SO_4^{2-}$ occurs and
614 the profiles generally match the data.

615 Clearly, a cross-plot showing 2:1 slope for in $\Delta Alk^*:\Delta SO_4^{2-}$ above the SMT
616 concentration does not imply organoclastic consumption of SO_4^{2-} . It can result from
617 multiple combinations of fluid flux with AOM and a deep source of DIC (from
618 methanogenesis). More interestingly, changes in the fluid flux or the rate of
619 methanogenesis and deep source DIC concentration can affect the slope (**Figure 9a**).

620 An increase in upward fluid flux (greater magnitude of Pe_2) will generally decrease the
621 slope on a $\Delta\text{Alk}^*:\Delta\text{SO}_4^{2-}$ cross-plot. This is because the SMT shoals (**Figure 4**) and also
622 high flux of DIC enters the SMT from depth. By contrast, an increase in methanogenesis
623 (higher Da) and a higher concentration of DIC at depth will generally increase the slope
624 (**Figure 9a**). This is because a greater concentration of DIC at depth as a result of
625 methanogenesis can then enter the SMT through advection and diffusion.

626 Simulated profiles for Site KC151-3 consistently render points that lie beneath a
627 2:1 slope; in fact, the slope in $\Delta\text{Alk}^*:\Delta\text{SO}_4^{2-}$ is less than 1:1 (**Figure 9b**). This reflects the
628 dual facts that a portion of DIC leaves the SMT to accumulate as carbonate beneath
629 this horizon, and that excess Ca^{2+} enters shallow sediment from below. An increase in
630 upward fluid flux would decrease the slope of the cross-plot similar to our above result
631 shown at Site 1244 (**Figure 9a**). In any case, the slope of the line does not indicate the
632 reaction.

633

634 4.4 Flux cross-plots

635 In contrast to using $\Delta\text{Alk}^*:\Delta\text{SO}_4^{2-}$ cross-plots, concentration gradients of alkalinity
636 (DIC), SO_4^{2-} and Ca^{2+} in and out of the SMT might be used to evaluate the role of AOM
637 [Luff and Wallman, 2003; Snyder et al., 2007; Dickens and Snyder, 2009; Kim et al.,
638 2011]. The basic idea is that the gradients are proportional to fluxes, so that the sum of
639 changes across the SMT should balance.

640 Starting from our simulated results, we compute concentration gradients by
641 linearly fitting the profiles above and below the SMT. Using these gradients, and
642 multiplying by sediment diffusion coefficients, we compute diffusive fluxes of CH_4 , SO_4^{2-}

643 and DIC across the SMT horizon. Advective flux of any dissolved species is a function
644 of fluid flux and the solute concentration. In the vicinity of the SMT, both the CH₄ and
645 SO₄²⁻ concentrations approach zero. Thus, in the vicinity of the SMT both the transport
646 of CH₄ and SO₄²⁻ are diffusion-dominated. Furthermore, the net advective DIC flux
647 across the SMT is calculated as a difference in deeper flux from/to deeper sediment and
648 shallow flux to/from the seafloor. Across the SMT, this net advective DIC flux is zero as
649 the individual deep and shallow advective DIC fluxes are equal and opposite in sign.
650 Hence, the total flux (sum of advective and diffusive flux) is equal to the diffusive flux
651 across the SMT.

652 The diffusive fluxes of CH₄ and DIC are now plotted relative to the SO₄²⁻ flux
653 (**Figure 10**). Crucially, this cross-plot (**Figure 10**) not only represents a diffusive flux
654 cross-plot, but it is also equivalent to a net flux cross-plot for a given pair of species.
655 Both CH₄ and DIC fluxes show a unique 1:1 correspondence relative to the SO₄²⁻ flux.
656 This 1:1 correspondence implies dominance of the AOM at the SMT, due to its
657 stoichiometric balance (**Equation 1**). Increasing the reaction rate of organoclastic
658 sulfate reduction (Da_{POC}) by few orders of magnitude ($\sim 10^2$) does not alter the slope of
659 the flux cross-plot (**Figure 10**). Interestingly, increasing the rate of methanogenesis
660 (Da) and a high DIC source at depth also correspond to a 1:1 relation between
661 respective fluxes. In essence, the difference between DIC flux leaving the SMT toward
662 the seafloor and the flux entering the SMT from below is equal to the flux added at the
663 SMT by AOM. This DIC flux added due to AOM at the SMT corresponds to the SO₄²⁻
664 flux entering the SMT from above by a simple 1:1 correlation, again because of the
665 stoichiometric relationship between CH₄, DIC, and SO₄²⁻ (**Equation 1**). In all these

666 cases the rate of downward SO_4^{2-} flux via diffusion is able to keep pace with CH_4
667 delivery from below, allowing DIC fluxes to also balance across the SMT.

668

669 *4.5 Relationship between AOM and $\delta^{13}\text{C}$ values*

670 The data show a wide range in $\delta^{13}\text{C}$ values of DIC at the SMT in shallow
671 sediment of gas hydrate systems (**Figure 2**). A series of papers have used this to
672 discriminate between potential causes for pore-water SO_4^{2-} consumption [*Claypool et*
673 *al.*, 2006; *Kastner et al.*, 2008a; *Torres and Kastner*, 2009]. The basic idea has been
674 that the $\delta^{13}\text{C}$ of DIC at the SMT relates to the relative proportion of DIC generated
675 through AOM and organoclastic sulfate reduction (**Equations 1 and 2**); the first reaction
676 would produce DIC exceptionally depleted in ^{13}C ($\delta^{13}\text{C} < -40\%$, depending on the CH_4
677 source) whereas the second reaction would produce DIC moderately depleted in ^{13}C
678 ($\delta^{13}\text{C} \sim -23\%$), roughly corresponding the $\delta^{13}\text{C}$ values of POC.

679 This approach, however, is fundamentally flawed because it neglects other inputs
680 (and outputs) of DIC to the SMT, especially DIC rising from depth. At most locations
681 including Sites 1244 and KC151-3, the CH_4 is derived from methanogenesis
682 (**Equations 3 and Appendix B**). As such, both ^{13}C -depleted CH_4 and ^{13}C -enriched DIC
683 are generated [e.g., *Conrad*, 2005], and the latter can enter and leave the SMT through
684 advection and diffusion. The $\delta^{13}\text{C}$ of DIC at the SMT, therefore, depends on the mixing
685 of DIC with different carbon isotope compositions. Our simulations clearly show that a
686 range of DIC $\delta^{13}\text{C}$ can (and should) occur across the SMT, even when AOM consumes
687 all SO_4^{2-} in shallow sediment.

688

689 4.6 Influence of Carbonate Precipitation

690 Methane-charged sediment deposited on modern continental margins (including
691 Cascadia Margin and the Gulf of Mexico) often contains authigenic carbonate [e.g., *Botz*
692 *et al.*, 1988; *Greinert et al.*, 2001; *Formolo et al.*, 2004]. Certainly, some of this
693 carbonate precipitates at or near an SMT [e.g., *Rodriguez et al.*, 2000; *Snyder et al.*,
694 2007], consistent with our model (**Figure 4** and **5**). Authigenic carbonate has also been
695 found in sedimentary rocks deposited along ancient continental margins that
696 presumably contained high CH₄ concentrations [e.g., *Campbell*, 2006]. Various lines of
697 evidence (e.g., biomarkers) suggest that some of this carbonate formed in association
698 with AOM [*Peckmann and Thiel*, 2004; *Allison et al.*, 2008].

699 Authigenic carbonates, both modern and ancient, exhibit a wide range in $\delta^{13}\text{C}$
700 [e.g., *Greinert et al.*, 2001; *Campbell*, 2006]. Various workers have generally attributed
701 this spread to the relative inputs of HCO₃⁻ from AOM, the oxidation of higher
702 hydrocarbons, and organoclastic sulfate reduction [*Botz et al.*, 1988; *Greinert et al.*,
703 2001; *Formolo et al.*, 2004; *Peckmann and Thiel*, 2004; *Campbell*, 2006; *Allison et al.*,
704 2008]. Our model results highlight a basic problem with this approach. As discussed for
705 pore water, carbonate precipitating at or near the SMT should have a wide range in
706 $\delta^{13}\text{C}$, even when AOM is the proximal cause for carbonate precipitation. Vertical inputs
707 and outputs of DIC to and from the SMT must be considered.

708

709 5. Conclusions

710 We have updated a 1-D numerical model for the formation of gas hydrate in
711 marine sediment [*Bhatnagar et al.*, 2007, 2008, 2011] so that it has coupled mass

712 balance equations for CH_4 , SO_4^{2-} , DIC, Ca^{2+} and the $\delta^{13}\text{C}$ of CH_4 and DIC in pore water.
713 This is an important progression because concentrations and carbon isotopic
714 composition of these species must be impacted collectively if CH_4 cycling in marine gas
715 hydrate systems includes sediment burial, CH_4 production from organic carbon, an
716 upward flux of methane, and significant loss of CH_4 by AOM. Moreover differences in
717 key parameters, including solute transport from deeper sediment through advection and
718 diffusion, should cause significant variations in the pore water chemistry of shallow
719 sediment.

720 Model simulations were conducted at two locations: Site 1244 (Hydrate Ridge)
721 and Site KC151-3 (Gulf of Mexico). We chose these locations because they have very
722 different DIC concentrations and $\delta^{13}\text{C}$ of DIC across the SMT. At both sites, the
723 simulations give good first-order descriptions for the profiles of CH_4 , SO_4^{2-} , DIC, Ca^{2+}
724 and the $\delta^{13}\text{C}$ of CH_4 and DIC in shallow sediment (**Figure 4** and **5**). Importantly, model
725 results are constrained by field measurements of physical and chemical parameters,
726 and the concentrations and shapes of model profiles. Crucially, the concentrations and
727 shapes of various profiles stem from coupled mass balance equations and site-specific
728 parameters; in other words, the inputs and outputs of CH_4 drive the profiles. Although
729 problems with our model remain (e.g., changing water activity, sediment
730 heterogeneities, lateral flow), the fact that CH_4 distributions and multiple pore water
731 profiles can be simulated simultaneously and fairly accurately at different locations
732 supports the approach.

733 Our numerical modeling gives a mathematically robust, process-based
734 explanation for SMT depth as well as the difference in carbon chemistry across the SMT

735 at Sites 1244 and KC151-3. At both sites, an upward flux of dissolved CH₄ reacts with
736 dissolved SO₄²⁻ at the SMT via AOM. Moreover, at both sites, AOM dominates the *net*
737 consumption of SO₄²⁻ in shallow sediment. At Site 1244, however, a high flux of ¹³C-
738 enriched DIC, produced by methanogenesis at depth, enters the SMT from below. This
739 is not the case at Site KC151-3, where a flux of ¹³C-enriched DIC leaves the SMT in
740 both directions. As such, the SMT has relatively high concentrations of moderately ¹³C-
741 depleted DIC at Site 1244 and relatively low concentrations of very ¹³C-depleted DIC at
742 Site KC151-3. Other factors, notably fluid flow and carbonate precipitation, secondarily
743 affect the carbon chemistry across the SMT at these sites. In any case, the differences
744 in DIC concentration and δ¹³C of DIC do not relate to the relative importance of AOM
745 and organoclastic sulfate reduction.

746 Cross-plots showing changes in alkalinity and SO₄²⁻ concentrations have been
747 used to assess the relative influence of AOM in marine sediment. The δ¹³C of DIC and
748 the δ¹³C of carbonate also have been used for this purpose. These approaches are not
749 appropriate for open systems without additional information, especially those where
750 large fluxes of ¹³C-enriched DIC enter shallow sediment from depth. Wide deviations in
751 ΔAlk*: ΔSO₄²⁻ slopes and DIC δ¹³C are expected, even when AOM consumes all *net*
752 SO₄²⁻ (**Figure 2**).

753 The DIC concentration and δ¹³C of DIC across the SMT exhibit broad ranges for
754 locations with underlying gas hydrate (**Figure 2**). On the basis of preliminary flux
755 arguments [*Dickens and Snyder, 2009*] and results presented here, we suspect this
756 range mostly signifies differences in fluid flux regime, and the relative proportions of ¹³C-
757 depleted CH₄ and ¹³C-enriched DIC entering the SMT.

758

759 **Appendices**

760 **Appendix A: Nomenclature**

761	c_i^j, \tilde{c}_i^j	Mass fraction of component i and normalized value in phase j
762	$c_{m,eqb}$	Equilibrium CH ₄ mass fraction in pore water at the base of the
763		GHSZ
764	$c_{s,o}, c_{b,o}, c_{Ca,o}$	Mass fraction of SO ₄ ²⁻ , DIC, and Ca ²⁺ in seawater
765	D_m, D_s, D_b, D_{Ca}	Diffusivities of CH ₄ , SO ₄ ²⁻ , DIC, and Ca ²⁺
766	Da_{AOM}, Da_{POC}, Da	Damköhler numbers for AOM, organoclastic sulfate reduction and
767		methanogenesis
768	dT/dz	Geothermal gradient
769	L_t, L_z	Depth to the base of the GHSZ, and simulation domain respectively
770	L_s, L_ϕ	SMT and compaction depth respectively
771	M_{CH_4}, M_{SO_4}	Molecular weight of CH ₄ , and SO ₄ ²⁻ respectively
772	$M_{HCO_3}, M_{Ca}, M_{POC}$	Molecular weight of DIC, Ca ²⁺ and POC, respectively
773	P_o	Hydrostatic pressure at the seafloor
774	Pe_1, Pe_2	Peclet numbers for compaction driven and external fluid flow
775	r	Reaction rate constant
776	\dot{s}	Sedimentation rate at the seafloor
777	t, \tilde{t}	Dimensional and dimensionless time, respectively
778	T_o	Seafloor temperature
779	U_f, U_{sed}	Net fluid flux and sediment flux, respectively

780	$\tilde{U}_f, \tilde{U}_{sed}$	Dimensionless net fluid flux and sediment flux, respectively
781	$U_{f, sed}, U_{f, ext}$	Fluid flux due to sedimentation and compaction, and upward flow,
782		respectively
783	v_s	Sediment velocity
784	z, \tilde{z}	Vertical depth and normalized vertical depth, respectively
785	$\alpha, \tilde{\alpha}$	Organic content in sediment and normalized value, respectively
786	α_o, β	Organic content at seafloor and normalized value, respectively
787	$\delta^{13}C_{POC}$	$\delta^{13}C$ of POC
788	$\delta^{13}C_{CH_4}, \delta^{13}C_{HCO_3}$	$\delta^{13}C$ of CH_4 and DIC, respectively
789	$\delta^{13}C_{CH_4, meth}$	$\delta^{13}C$ of CH_4 generated by methanogenesis
790	$\delta^{13}C_{HCO_3, meth}$	$\delta^{13}C$ of DIC generated by methanogenesis
791	$\delta^{13}C_{HCO_3, POC}$	$\delta^{13}C$ of DIC produced by organoclastic sulfate reduction
792	ε_m	Fractionation factor for methanogenesis
793	$\phi, \tilde{\phi}$	Sediment porosity and reduced sediment porosity, respectively
794	ϕ_o, ϕ_∞	Sediment porosity at the seafloor and minimum porosity at depth,
795		respectively
796	γ, η	Reduced porosity parameters
797	$\lambda_{AOM}, \lambda_{POC}, \lambda$	Rates of AOM, organoclastic sulfate reduction and methanogenesis
798	$\rho_j, \tilde{\rho}_j$	Density of the phase j and normalized value, respectively
799		
800	Subscripts and superscripts:	

801	<i>w, m, s</i>	Water, CH ₄ and SO ₄ ²⁻ components, respectively
802	<i>b, Ca, CaCO₃</i>	DIC, Ca ²⁺ and CaCO ₃ components, respectively
803	<i>l, sed</i>	Liquid and sediment phase, respectively
804	<i>AOM, POC</i>	AOM and organoclastic sulfate reduction reactions, respectively
805	<i>meth, ppt</i>	Methanogenesis and calcite precipitation reactions, respectively

806

807 **Appendix B: Chemical reactions**

808 Methanogenesis is complex but can be represented with a simplified set of
809 reactions [e.g., *Conrad, 2005*]

810 *Fermentation:*



812 *CO₂ reduction and acetate methanogenesis*



815 *Overall reaction:*



817 The carbon dioxide generated will react with pore water to form DIC:



819 Carbon isotope fractionation during methanogenesis is also complex and
820 depends on the composition of precursors, various fractionation factors, and the relative
821 contribution of methanogenic pathways [e.g., *Conrad, 2005*]. By combining fermentation

822 and both pathways for methanogenesis (**Equations B1-B4**), we have implicitly
823 integrated carbon isotope fractionation within intermediate reactions.

824

825 **Appendix C: Updated Model Equations**

826 C.1 Mass balances

827 C.1.1 Organic carbon

828 During sediment burial, microbes use a portion of POC in chemical reactions. We
829 define this labile (utilizable) organic carbon as α . For this work, the reactions are
830 methanogenesis (**Equation 3**) and organoclastic sulfate consumption (**Equation 5**).
831 The overall mass balance equation for labile organic carbon is:

$$832 \quad \frac{\partial}{\partial t} [1 - \phi \rho_{sed} \alpha] + \frac{\partial}{\partial z} [1 - \phi \rho_{sed} v_s \alpha] = -\rho_{sed} \lambda (1 - \phi) \alpha - \frac{\phi (1 - \phi)}{M_{SO_4}} \lambda_{POC} (\rho_{sed} \alpha) (\rho_w c_s^I), \quad (\mathbf{C1})$$

833 where ρ_{sed} = sediment density, ρ_w = water density, z = depth, v_s = sediment velocity,
834 c_s^I = dissolved SO_4^{2-} concentration, λ = first-order rate constant of methanogenesis
835 (**Equation 3**), ϕ = porosity, M_{SO_4} = molecular weight of SO_4^{2-} , and λ_{POC} = second-order
836 rate constant of organoclastic sulfate reduction (**Equation 5**).

837 The two terms on the left of **Equation C1** represent the accumulation of labile
838 organic carbon with time, and divergence of the transport of this component with depth.
839 The two terms on the right correspond to the reactions that consume labile POC
840 (**Equations 3 and 5**, respectively). Note three simplifications: the amount of degradable
841 POC at the seafloor is constant with time; organic carbon is buried (down) with v_s
842 equivalent to the sedimentation rate (\dot{S}); and the sedimentation rate is constant over
843 time.

844

845 C.1.2 Methane

846 Once CH₄ forms in sediment, it can accumulate as dissolved gas, gas hydrate, or
847 free gas. In a dynamic system, CH₄ also moves with respect to the seafloor over time. It
848 can advect down with sediment (burial) as gas hydrate, advect up or down with fluid as
849 dissolved or free gas, or diffuse due to concentration gradients in the dissolved phase. It
850 can also rise as free gas; however, free gas migration is not modeled in this study (*n.b.*,
851 compelling evidence for free gas migration through the GHSZ does not exist at the sites
852 examined; e.g., *Cook et al.*, 2008; *Lee and Collett*, 2008). Furthermore, dissolved CH₄
853 transported towards the seafloor can react with SO₄²⁻ (**Equation 4**). The overall mass
854 balance equation for dissolved CH₄ is:

855
$$\frac{\partial}{\partial t} [\phi \rho_w c_m^l] + \frac{\partial}{\partial z} [U_f \rho_w c_m^l] = \frac{\partial}{\partial z} \left[\phi \rho_w D_m \frac{\partial c_m^l}{\partial z} \right] + \frac{M_{CH_4}}{M_{POC}} \rho_{sed} \lambda (1 - \phi) \alpha - \frac{\phi \lambda_{AOM} (\rho_w c_m^l)(\rho_w c_s^l)}{M_{SO_4}},$$

856 **(C2)**

857 where U_f = net fluid flux, c_m^l = dissolved CH₄ concentration, λ_{AOM} = AOM reaction rate
858 constant (**Equation 4**), D_m = CH₄ diffusivity, M_{CH_4} and M_{POC} = molecular weights of
859 CH₄ and POC, respectively (and other parameters are defined above). The net fluid flux
860 U_f is the sum of the fluid flux due to sedimentation (i.e., that carried down in pore space
861 through burial and compaction) and the external fluid flux (i.e., that moved relative to the
862 sediment from deeper sources).

863 The two terms on the left of **Equation C2** represent the accumulation and
864 divergence of CH₄ advection; the three terms on the right correspond to CH₄ diffusion,
865 methanogenesis (**Equation 3**), and AOM (**Equation 4**). Methane production and

866 concentration are assumed zero at and above the SMT. Hence, methanogenesis in the
 867 model only occurs in the absence of pore water SO_4^{2-} .

868 The mass balance equations in *Bhatnagar et al.* [2007, 2008] include three
 869 phases for CH_4 (e.g., dissolved, hydrate, and free gas). In this study, we neglect the
 870 hydrate and free gas phases in our calculations, and only solve for the dissolved CH_4
 871 concentration (basically, CH_4 concentrations exceeding solubility do not form gas
 872 hydrate or free gas). This simplifies the model, and allows us to focus on shallow pore
 873 water chemistry profiles, the primary concern of this paper. This simplification also does
 874 not affect the remaining pore water chemistry profiles (e.g., SO_4^{2-} , DIC, Ca^{2+}) as they
 875 are all dissolved species and only relate to the dissolved phase concentration of CH_4 .

876

877 C.1.3 Sulfate

878 Deep ocean SO_4^{2-} concentrations have been a constant value, ~28 mM, for
 879 millions of years [*Lowenstein et al.*, 2001], with the exception of anoxic zones. With
 880 sediment burial, however, pore water SO_4^{2-} concentrations can vary significantly
 881 (**Figure 3a**) because of fluid advection, diffusion, and two consumption reactions
 882 (**Equations 4** and **5**). The overall SO_4^{2-} mass balance equation that incorporates these
 883 factors is:

$$\begin{aligned}
 884 \quad & \frac{\partial}{\partial t} [\phi \rho_w c_s^l] + \frac{\partial}{\partial z} [U_f \rho_w c_s^l] = \frac{\partial}{\partial z} \left[\phi \rho_w D_s \frac{\partial c_s^l}{\partial z} \right] \\
 885 \quad & - \frac{\phi \lambda_{AOM} (\rho_w c_m^l) (\rho_w c_s^l)}{M_{CH_4}} - \frac{\phi (1-\phi) \lambda_{POC} (\rho_{sed} \alpha) (\rho_w c_s^l)}{M_{POC}}, \quad (\text{C3})
 \end{aligned}$$

886 where D_s = sulfate diffusivity (and other parameters are defined above).

887 The two terms on the left of **Equation C3** represent the accumulation and
 888 divergence of SO_4^{2-} advection; the three terms on the right correspond to SO_4^{2-}
 889 diffusion, AOM, and organoclastic sulfate reduction, respectively.

890

891 C.1.4 Dissolved inorganic carbon (DIC)

892 The DIC of deep-ocean water has also been fairly constant on long timescales
 893 [Lowenstein *et al.*, 2001]. However, like SO_4^{2-} , several processes can change its
 894 concentration in pore water (**Figure 3b**). Transport by advection and diffusion occurs,
 895 as well as production by methanogenesis (**Equation 3**), AOM (**Equation 4**),
 896 organoclastic sulfate reduction (**Equation 5**), and removal by carbonate precipitation
 897 (**Equation 6**). The overall DIC mass balance equation is:

$$\begin{aligned}
 898 \quad \frac{\partial}{\partial t} [\phi \rho_w c_b^I] + \frac{\partial}{\partial z} [U_f \rho_w c_b^I] = \frac{\partial}{\partial z} \left[\phi \rho_w D_b \frac{\partial c_b^I}{\partial z} \right] + \frac{M_{\text{HCO}_3}}{M_{\text{POC}}} \rho_{\text{sed}} \lambda (1 - \phi) \alpha \\
 899 \quad + \frac{M_{\text{HCO}_3} \phi \lambda_{\text{AOM}} (\rho_w c_m^I) (\rho_w c_s^I)}{M_{\text{CH}_4} M_{\text{SO}_4}} + \frac{2M_{\text{HCO}_3} \phi (1 - \phi) \lambda_{\text{POC}} (\rho_{\text{sed}} \alpha) (\rho_w c_s^I)}{M_{\text{POC}} M_{\text{SO}_4}} - \phi \rho_w \frac{\Delta c_{\text{CaCO}_3}}{\Delta t}, \quad (\text{C4})
 \end{aligned}$$

900 where c_b^I = DIC concentration, D_b = DIC diffusivity, and M_{HCO_3} = molecular weight of
 901 DIC, c_{CaCO_3} = concentration of CaCO_3 precipitated (and other parameters are defined
 902 above).

903 The two terms on the left of **Equation C4** represent the accumulation and
 904 divergence of DIC advection; the five terms on the right correspond to diffusion,
 905 followed by the three reactions that generate DIC (**Equations 3-5**), and the one reaction
 906 that consumes DIC (**Equation 6**). The DIC mass balance equation does not imply that

907 all DIC will be consumed in sediment. In fact, as will be shown, significant loss of DIC to
908 the ocean can occur through the sediment-water interface.

909

910 C.1.5 Calcium

911 Dissolved Ca^{2+} concentrations of deep ocean water have also been relatively
912 constant on long timescales [Lowenstein *et al.*, 2001], but often change in sediment
913 (**Figure 3c**) because of advection, diffusion, and carbonate precipitation. The Ca^{2+}
914 mass balance equation is:

$$915 \quad \frac{\partial}{\partial t} [\phi \rho_w c_{Ca}^l] + \frac{\partial}{\partial z} [U_f \rho_w c_{Ca}^l] = \frac{\partial}{\partial z} \left[\phi \rho_w D_{Ca} \frac{\partial c_{Ca}^l}{\partial z} \right] - \phi \rho_w \frac{\Delta c_{CaCO_3}}{\Delta t}, \quad (\text{C5})$$

916 where c_{Ca}^l = dissolved Ca^{2+} concentration, and D_{Ca} = Ca^{2+} diffusivity (and other
917 parameters are defined above).

918 The two terms on the left of **Equation C5** represent the accumulation and
919 divergence of Ca^{2+} advection; the two terms on the right correspond to Ca^{2+} diffusion
920 and carbonate precipitation (**Equation 6**). As mentioned earlier, carbonate precipitation
921 has been modeled as an equilibrium reaction with calcite as the mineral precipitate.

922

923 C.1.6 Carbon isotopic composition

924 The carbon isotope composition ($\delta^{13}\text{C}$) of methane and DIC clearly change in
925 sediment (**Figure 3d**). Consequently, the ^{12}C and ^{13}C contents of these carbon-bearing
926 phases should be tracked, for which there are two main considerations. POC buried
927 with sediment has a $\delta^{13}\text{C}$ between -26 and -16‰ [Conrad, 2005; Kim *et al.*, 2007].
928 During methanogenesis, however, fractionation of carbon isotope values occurs, such

929 that the CH₄ becomes depleted in ¹³C while the DIC becomes enriched in ¹³C [e.g.,
 930 Conrad, 2005].

931 For CH₄, we incorporate carbon isotopes into **Equation C2** as follows:

$$\begin{aligned}
 932 \quad & \frac{\partial}{\partial t} [\phi \rho_w c_m^l \delta^{13}C_{CH_4}] + \frac{\partial}{\partial z} [U_f \rho_w c_m^l \delta^{13}C_{CH_4}] = \frac{\partial}{\partial z} \left[\phi \rho_w D_m \frac{\partial (c_m^l \delta^{13}C_{CH_4})}{\partial z} \right] \\
 933 \quad & + \frac{M_{CH_4}}{M_{POC}} \rho_{sed} \lambda (1 - \phi) \alpha \delta^{13}C_{CH_4, meth} - \frac{\phi \lambda_{AOM} (\rho_w c_m^l) (\rho_w c_s^l) \delta^{13}C_{CH_4}}{M_{SO_4}}, \quad (C6)
 \end{aligned}$$

934 where $\delta^{13}C_{CH_4} = \delta^{13}C$ of dissolved CH₄, and $\delta^{13}C_{CH_4, meth} = \delta^{13}C$ of CH₄ produced during
 935 methanogenesis (fixed site-specific parameter).

936 Likewise for DIC, we incorporate carbon isotope values into **Equation C4** as
 937 follows:

$$\begin{aligned}
 938 \quad & \frac{\partial}{\partial t} [\phi \rho_w c_b^l \delta^{13}C_{HCO_3}] + \frac{\partial}{\partial z} [U_f \rho_w c_b^l \delta^{13}C_{HCO_3}] = \frac{\partial}{\partial z} \left[\phi \rho_w D_b \frac{\partial (c_b^l \delta^{13}C_{HCO_3})}{\partial z} \right] \\
 939 \quad & + \frac{M_{HCO_3}}{M_{POC}} \rho_{sed} \lambda (1 - \phi) \alpha \delta^{13}C_{HCO_3, meth} + \frac{M_{HCO_3} \phi \lambda_{AOM} (\rho_w c_m^l) (\rho_w c_s^l) \delta^{13}C_{CH_4}}{M_{CH_4} M_{SO_4}} \\
 940 \quad & + \frac{2M_{HCO_3} \phi (1 - \phi) \lambda_{POC} (\rho_{sed} \alpha) (\rho_w c_s^l) \delta^{13}C_{HCO_3, POC}}{M_{POC} M_{SO_4}} - \phi \rho_w \frac{\Delta (c_{CaCO_3} \delta^{13}C_{HCO_3})}{\Delta t}, \quad (C7)
 \end{aligned}$$

941 where $\delta^{13}C_{HCO_3} = \delta^{13}C$ of dissolved DIC, $\delta^{13}C_{HCO_3, meth} = \delta^{13}C$ of DIC generated by
 942 methanogenesis (a fixed, site-specific parameter), and $\delta^{13}C_{HCO_3, POC} = \delta^{13}C$ of DIC
 943 generated by sulfate reduction of POC (a fixed, site-specific parameter).

944 The two terms on the left of **Equation C7** represent the accumulation and
 945 divergence of advection of ¹²C and ¹³C in DIC; the five terms on the right correspond to

946 the diffusion of ^{12}C and ^{13}C in DIC, followed by the three reactions that generate DIC
947 (**Equations 3-5**), and the one that consumes DIC (**Equation 6**).

948

949 *C.2 Normalized variables and key dimensionless groups*

950 The mass balance equations (**Equations C1-C7**) can be rewritten in
951 dimensionless form [*Bhatnagar et al.*, 2007, 2008]. This reduces the number of
952 parameters describing a particular system, and allows for straightforward comparisons
953 of different systems from a mechanistic perspective. To accomplish this, key variables
954 need to be normalized. We follow the scaling schemes developed by *Bhatnagar et al.*
955 [2007]. All dimensionless variables are represented with a tilde ($\tilde{\cdot}$) to distinguish them
956 from their corresponding dimensional forms.

957 Vertical depth is scaled to the base of the GHSZ (L_t):

$$958 \quad \tilde{z} = \frac{z}{L_t}. \quad (\text{C8})$$

959 This means that, for all gas hydrate systems examined, various calculations are made
960 and results presented with the seafloor and the base of the GHSZ having values of 0
961 and 1, respectively (e.g., **Figures 4 and 5**).

962 Time is normalized through a combination of L_t and diffusivity of methane (D_m).

$$963 \quad \tilde{t} = \frac{t}{L_t^2/D_m}. \quad (\text{C9})$$

964 Initial time is denoted by $\tilde{t} = 0$ when sediments start to land on the seafloor. Normalized
965 time $\tilde{t} = 1$ implies the diffusion time required to travel the distance between the base of
966 the GHSZ and the seafloor.

967 Contents of degradable POC in the sediment column (α) are normalized to the
 968 initial quantity deposited at the seafloor (α_0). The initial POC content deposited at the
 969 seafloor is normalized with the equilibrium CH₄ concentration at the base of GHSZ
 970 ($c_{m,eqb}$). These are expressed as:

$$971 \quad \tilde{\alpha} = \frac{\alpha}{\alpha_0}, \quad \beta = \frac{\alpha_0}{c_{m,eqb}}. \quad (\text{C10})$$

972 Likewise, dissolved CH₄ concentrations through the sediment column (c_m^l) are
 973 normalized to the equilibrium CH₄ concentration at the base of GHSZ. This is because,
 974 for the upper few hundreds of meters of marine sediment, the maximum possible c_m^l will
 975 typically occur at this depth [Zatsepina and Buffett, 1998; Bhatnagar et al., 2007];
 976 **Figure 1a**). The normalization is expressed as:

$$977 \quad \tilde{c}_m^l = \frac{c_m^l}{c_{m,eqb}}. \quad (\text{C11})$$

978 By contrast, pore water SO₄²⁻, DIC, and Ca²⁺ concentrations are normalized to
 979 their respective values in seawater, $c_{s,o}$, $c_{b,o}$, and $c_{Ca,o}$:

$$980 \quad \tilde{c}_s^l = \frac{c_s^l}{c_{s,o}}, \quad \tilde{c}_b^l = \frac{c_b^l}{c_{b,o}}, \quad \tilde{c}_{ca}^l = \frac{c_{ca}^l}{c_{Ca,o}}. \quad (\text{C12})$$

981 In general, normalized SO₄²⁻ and Ca²⁺ concentrations will diminish from 1 with depth,
 982 while normalized DIC concentrations will exceed 1 with depth (**Figures 4 and 5**).

983 Porosity at a given depth is normalized to the minimum value at great depth (ϕ_∞):

$$984 \quad \tilde{\phi} = \frac{\phi - \phi_\infty}{1 - \phi_\infty}. \quad (\text{C13})$$

985 However, to obtain appropriate porosity profile with depth and to simplify equations, two
 986 additional parameters are introduced:

$$987 \quad \eta = \frac{\phi_0 - \phi_\infty}{1 - \phi_\infty}, \quad \gamma = \frac{1 - \phi_\infty}{\phi_\infty}, \quad (\text{C14})$$

988 where ϕ_0 = porosity at the seafloor and η = normalized porosity at the seafloor. In
 989 general, porosity decreases with depth because of compaction, so that $\phi_0 > \phi > \phi_\infty$ and
 990 $\eta > \tilde{\phi}$. At great depth, porosity approaches a minimum value and the fluid and sediment
 991 velocities approach a common asymptotic value [*Berner, 1980; Davie and Buffett, 2001;*
 992 *Bhatnagar et al., 2007*]. Fluid gets buried (downward) with the sediment and its velocity
 993 increases with depth. However, the fluid flux (product of its velocity and porosity) at any
 994 depth remains constant at steady-state conditions.

995 The downward component of the net fluid flux (U_f), defined as $U_{f, sed}$, can be
 996 expressed as a combination of sedimentation rate (\dot{S}) and porosity parameters
 997 [*Bhatnagar et al., 2007*]:

$$998 \quad U_{f, sed} = \frac{1 - \phi_0}{1 - \phi_\infty} \dot{S} \phi_\infty. \quad (\text{C15})$$

999 The sediment flux (U_{sed}) can be defined as:

$$1000 \quad U_{sed} = 1 - \phi_0 \dot{S}. \quad (\text{C16})$$

1001 It represents the downward transport of sediment grains, and is assumed to be
 1002 constant. For convenience, it can be scaled with respect to $U_{f, sed}$, which can be related
 1003 to γ [*Bhatnagar et al., 2007*].

1004
$$\tilde{U}_{sed} = \frac{U_{sed}}{U_{f, sed}} = \frac{1 - \phi_o}{U_{f, sed}} \dot{S} = \frac{\left(\frac{1 - \phi_\infty}{\phi_\infty} \right) U_{f, sed}}{U_{f, sed}} = \left(\frac{1 - \phi_\infty}{\phi_\infty} \right) = \gamma. \quad (\text{C17})$$

1005 Other than through fluid burial, dissolved species can move through external fluid flow
 1006 and diffusion. The relative significance of these processes are perhaps best understood
 1007 by defining two dimensionless groups known as Peclet numbers. The first Peclet
 1008 number (Pe_1) we define characterizes the ratio of sediment-driven fluid flux to methane
 1009 diffusion:

1010
$$Pe_1 = \frac{U_{f, sed} L_t}{D_m}. \quad (\text{C18})$$

1011 By contrast, the second Peclet number (Pe_2) characterizes the ratio of external fluid flux
 1012 (generally upward from deeper sediment) to CH_4 diffusion:

1013
$$Pe_2 = \frac{U_{f, ext} L_t}{D_m}. \quad (\text{C19})$$

1014 These dimensionless numbers are scaled by CH_4 diffusion to enable quick comparison
 1015 of relative amounts of advection and diffusion of methane. Crucially, Pe_1 and Pe_2
 1016 typically act in downward and upward directions respectively, and have opposite signs.

1017 Another set of dimensionless groups, the Damköhler numbers, are also
 1018 convenient because they characterize the ratio of reaction to diffusion. Three
 1019 Damköhler numbers are defined here:

1020 Methanogenesis:
$$Da = \frac{\lambda L_t^2}{D_m}, \quad (\text{C20})$$

1021 AOM:
$$Da_{AOM} = \frac{\rho_w c_{m,eqb}}{M_{CH_4}} \frac{\lambda_{AOM} L_t^2}{D_m}, \quad (\text{C21})$$

1022 Organoclastic sulfate reduction:
$$Da_{POC} = \frac{\rho_w c_{m,eqb}}{M_{POC}} \frac{\lambda_{POC} L_t^2}{D_s}. \quad (\text{C22})$$

1023 All parameters and dimensionless groups are defined collectively, along with
1024 specific values in **Appendix A** and **Table 1**.

1025

1026 *C.3 Dimensionless mass balance equations*

1027 The dimensional mass balance equations (**Equations C1-C7**) can be rewritten in
1028 dimensionless form using the normalized variables and dimensionless groups defined
1029 above. The evolution of POC through depth and time can be expressed as:

1030
$$\frac{\partial}{\partial \tilde{t}} \tilde{\alpha}(1-\tilde{\phi}) + Pe_1 \frac{\partial}{\partial \tilde{z}} \left[\left(\frac{1+\gamma}{\gamma} \right) \tilde{U}_{sed} \tilde{\alpha} \right] = -Da(1-\tilde{\phi})\tilde{\alpha} - \frac{1-\tilde{\phi}}{1+\gamma} \frac{1+\gamma\tilde{\phi}}{D_m M_{SO_4} c_{m,eqb}} \frac{D_s M_{POC} c_{s,o}}{Da_{POC}} \tilde{\alpha} \tilde{c}_s^l.$$

1031 (C23)

1032 For CH₄, the dimensionless mass balance equation is:

1033
$$\frac{\partial}{\partial \tilde{t}} \left[\left(\frac{1+\gamma\tilde{\phi}}{\gamma} \right) \tilde{c}_m^l \right] + \left(\frac{1+\gamma}{\gamma} \right) (Pe_1 + Pe_2) \frac{\partial \tilde{c}_m^l}{\partial \tilde{z}} = \frac{\partial}{\partial \tilde{z}} \left[\left(\frac{1+\gamma\tilde{\phi}}{\gamma} \right) \frac{\partial \tilde{c}_m^l}{\partial \tilde{z}} \right]$$

1034
$$+ \frac{M_{CH_4}}{M_{POC}} \tilde{\rho}_{sed} Da \frac{1-\tilde{\phi}}{\tilde{\alpha} \beta} - \left(\frac{1+\gamma\tilde{\phi}}{\gamma} \right) \frac{M_{CH_4} c_{s,o}}{M_{SO_4} c_{m,eqb}} Da_{AOM} \tilde{c}_m^l \tilde{c}_s^l. \quad (\text{C24})$$

1035 For SO₄²⁻:

1036
$$\frac{\partial}{\partial \tilde{t}} \left[\left(\frac{1+\gamma\tilde{\phi}}{\gamma} \right) \tilde{c}_s^l \right] + \left(\frac{1+\gamma}{\gamma} \right) (Pe_1 + Pe_2) \frac{\partial \tilde{c}_s^l}{\partial \tilde{z}} = \frac{\partial}{\partial \tilde{z}} \left[\left(\frac{1+\gamma\tilde{\phi}}{\gamma} \right) \frac{D_s}{D_m} \frac{\partial \tilde{c}_s^l}{\partial \tilde{z}} \right]$$

$$1037 \quad -\left(\frac{1+\gamma\tilde{\phi}}{\gamma}\right)Da_{AOM}\tilde{c}_m^l\tilde{c}_s^l - \frac{1-\tilde{\phi}}{1+\gamma}\frac{1+\gamma\tilde{\phi}}{D_m}D_s\tilde{\rho}_{sed}Da_{POC}\tilde{\alpha}\beta\tilde{c}_s^l. \quad (\text{C25})$$

1038 For DIC:

$$1039 \quad \frac{\partial}{\partial \tilde{t}}\left[\left(\frac{1+\gamma\tilde{\phi}}{\gamma}\right)\tilde{c}_b^l\right] + \left(\frac{1+\gamma}{\gamma}\right)(Pe_1 + Pe_2)\frac{\partial \tilde{c}_b^l}{\partial \tilde{z}} = \frac{\partial}{\partial \tilde{z}}\left[\left(\frac{1+\gamma\tilde{\phi}}{\gamma}\right)\frac{D_b}{D_m}\frac{\partial \tilde{c}_b^l}{\partial \tilde{z}}\right]$$

$$1040 \quad + \frac{M_{HCO_3}c_{m,eqb}}{M_{POC}c_{b,o}}\tilde{\rho}_{sed}Da\frac{1-\tilde{\phi}}{1+\gamma}\tilde{\alpha}\beta + \left(\frac{1+\gamma\tilde{\phi}}{\gamma}\right)\frac{M_{HCO_3}c_{s,o}}{M_{SO_4}c_{b,o}}Da_{AOM}\tilde{c}_m^l\tilde{c}_s^l$$

$$1041 \quad + \frac{2M_{HCO_3}c_{s,o}}{M_{SO_4}c_{b,o}}\frac{1-\tilde{\phi}}{1+\gamma}\frac{1+\gamma\tilde{\phi}}{D_m}D_s\tilde{\rho}_{sed}Da_{POC}\tilde{\alpha}\beta\tilde{c}_s^l - \left(\frac{1+\gamma\tilde{\phi}}{\gamma}\right)\frac{c_{Ca,o}}{c_{b,o}}\frac{\Delta\tilde{c}_{CaCO_3}}{\Delta\tilde{t}}. \quad (\text{C26})$$

1042 For Ca²⁺:

$$1043 \quad \frac{\partial}{\partial \tilde{t}}\left[\left(\frac{1+\gamma\tilde{\phi}}{\gamma}\right)\tilde{c}_{Ca}^l\right] + \left(\frac{1+\gamma}{\gamma}\right)(Pe_1 + Pe_2)\frac{\partial \tilde{c}_{Ca}^l}{\partial \tilde{z}} = \frac{\partial}{\partial \tilde{z}}\left[\left(\frac{1+\gamma\tilde{\phi}}{\gamma}\right)\frac{D_{Ca}}{D_m}\frac{\partial \tilde{c}_{Ca}^l}{\partial \tilde{z}}\right] - \left(\frac{1+\gamma\tilde{\phi}}{\gamma}\right)\frac{\Delta\tilde{c}_{CaCO_3}}{\Delta\tilde{t}}.$$

$$1044 \quad (\text{C27})$$

1045 For ¹²C and ¹³C of CH₄:

$$1046 \quad \frac{\partial}{\partial \tilde{t}}\left[\left(\frac{1+\gamma\tilde{\phi}}{\gamma}\right)\tilde{c}_m^l\delta^{13}C_{CH_4}\right] + \left(\frac{1+\gamma}{\gamma}\right)(Pe_1 + Pe_2)\frac{\partial}{\partial \tilde{z}}\left[\tilde{c}_m^l\delta^{13}C_{CH_4}\right] = \frac{\partial}{\partial \tilde{z}}\left[\left(\frac{1+\gamma\tilde{\phi}}{\gamma}\right)\frac{\partial}{\partial \tilde{z}}\left[\tilde{c}_m^l\delta^{13}C_{CH_4}\right]\right]$$

$$1047 \quad + \frac{M_{CH_4}}{M_{POC}}\tilde{\rho}_{sed}Da\frac{1-\tilde{\phi}}{1+\gamma}\tilde{\alpha}\beta\delta^{13}C_{CH_4,meth} - \left(\frac{1+\gamma\tilde{\phi}}{\gamma}\right)\frac{M_{CH_4}c_{s,o}}{M_{SO_4}c_{m,eqb}}Da_{AOM}\tilde{c}_m^l\tilde{c}_s^l\delta^{13}C_{CH_4}. \quad (\text{C28})$$

1048 And, for ¹²C and ¹³C of DIC:

$$1049 \quad \frac{\partial}{\partial \tilde{t}}\left[\left(\frac{1+\gamma\tilde{\phi}}{\gamma}\right)\tilde{c}_b^l\delta^{13}C_{HCO_3}\right] + \left(\frac{1+\gamma}{\gamma}\right)(Pe_1 + Pe_2)\frac{\partial}{\partial \tilde{z}}\left[\tilde{c}_b^l\delta^{13}C_{HCO_3}\right] = \frac{\partial}{\partial \tilde{z}}\left[\left(\frac{1+\gamma\tilde{\phi}}{\gamma}\right)\frac{D_b}{D_m}\frac{\partial}{\partial \tilde{z}}\left[\tilde{c}_b^l\delta^{13}C_{HCO_3}\right]\right]$$

$$1050 \quad + \frac{M_{HCO_3}c_{m,eqb}}{M_{POC}c_{b,o}}\tilde{\rho}_{sed}Da\frac{1-\tilde{\phi}}{1+\gamma}\tilde{\alpha}\beta\delta^{13}C_{HCO_3,meth} + \left(\frac{1+\gamma\tilde{\phi}}{\gamma}\right)\frac{M_{HCO_3}c_{s,o}}{M_{SO_4}c_{b,o}}Da_{AOM}\tilde{c}_m^l\tilde{c}_s^l\delta^{13}C_{CH_4}$$

1070 where σ_ϕ = characteristic constant with units of stress, and g = acceleration due to
 1071 gravity. In all our simulations, $N_{i\phi} = 1$, implying compaction depth (L_ϕ) is equal to the
 1072 thickness of the GHSZ (L_t). Unit compaction depth further implies porosity at this depth
 1073 is reduced by 1/e (or 36.8%) from its initial porosity at the seafloor.

1074 The labile organic carbon content (α) is assumed to be 0% throughout all
 1075 sediment at initial time $\tilde{t} = 0$. No CH₄ is present at this time in the sediment column, so
 1076 the CH₄ concentration (c_m^l) is zero. Therefore, the normalized labile organic content
 1077 ($\tilde{\alpha}$), and the CH₄ concentration (\tilde{c}_m^l) are zero (**Equation C32**).

$$1078 \quad \tilde{\alpha}(\tilde{z}, 0) = 0, \quad \tilde{c}_m^l(\tilde{z}, 0) = 0. \quad (\mathbf{C32})$$

1079 The pore water SO₄²⁻ (c_s^l), DIC (c_b^l), Ca²⁺ (c_{Ca}^l) concentrations, and the carbon
 1080 isotope compositions ($\delta^{13}C$) are assumed to be seawater values at initial time for any
 1081 depth \tilde{z} . The normalized pore water concentrations of SO₄²⁻ (\tilde{c}_s^l), DIC (\tilde{c}_b^l), and Ca²⁺
 1082 (\tilde{c}_{Ca}^l) are unity at $\tilde{t} = 0$ (**Equation C33**). At the same time, carbon isotope compositions
 1083 in CH₄ and DIC are zero because the carbon isotope compositions are normalized
 1084 relative to a marine carbonate standard.

$$1085 \quad \tilde{c}_s^l(\tilde{z}, 0) = \tilde{c}_b^l(\tilde{z}, 0) = \tilde{c}_{Ca}^l(\tilde{z}, 0) = 1, \quad \delta^{13}C_{CH_4}(\tilde{z}, 0) = \delta^{13}C_{HCO_3}(\tilde{z}, 0) = 0. \quad (\mathbf{C33})$$

1086 In essence, at $\tilde{t} = 0$, there is a sediment column with prescribed physical
 1087 conditions (i.e., temperature, pressure, and porosity). This column has no POC, and
 1088 pore space is filled with seawater. For all $\tilde{t} > 0$, POC is continuously deposited on the
 1089 seafloor. A fraction of this is labile and, upon burial, drives a sequence of chemical
 1090 reactions. These lead to changes in pore water CH₄, SO₄²⁻, DIC, and Ca²⁺

1091 concentrations, as well as the $\delta^{13}\text{C}$ of DIC. The amounts of CH_4 , DIC and Ca^{2+} are
1092 restricted because of solubility.

1093

1094 *C.5 Boundary conditions*

1095 As time progresses, pore water concentrations throughout the sediment column
1096 change from their initial values. We specify boundary values to all variables at the
1097 seafloor, and at the bottom of our simulation domain. Normalized labile POC content is
1098 unity at the seafloor. By contrast, due to very low CH_4 concentrations in seawater,
1099 normalized CH_4 concentration is zero at the seafloor. These boundary values are

1100 **(Equation C34):**

$$1101 \quad \tilde{\alpha}(0, \tilde{t}) = 1, \quad \tilde{c}_m^l(0, \tilde{t}) = 0. \quad (\text{C34})$$

1102 As discussed earlier, CH_4 concentration is also zero below the seafloor until the SMT.
1103 Importantly, however, we do not prescribe this as a boundary value. Instead, this
1104 condition arises in our model because minimal methanogenesis occurs in the presence
1105 of SO_4^{2-} , and because CH_4 reacts with SO_4^{2-} via AOM.

1106 At the seafloor, normalized pore water SO_4^{2-} , DIC and Ca^{2+} concentrations are
1107 unity, while normalized carbon isotope compositions in CH_4 and DIC are zero. These are

1108 **(Equation C35):**

$$1109 \quad \tilde{c}_s^l(0, \tilde{t}) = \tilde{c}_b^l(0, \tilde{t}) = \tilde{c}_{ca}^l(0, \tilde{t}) = 1, \quad \delta^{13}\text{C}_{\text{CH}_4}(0, \tilde{t}) = \delta^{13}\text{C}_{\text{HCO}_3}(0, \tilde{t}) = 0. \quad (\text{C35})$$

1110 Upward fluid flux is modeled so as to transport dissolved CH_4 , DIC, Ca^{2+} , and
1111 other pore water species from deeper sediments. Consequently, pore water
1112 concentrations need to be specified at the base of the simulation domain ($L_z = 2L_t$).

1113 Pore water CH₄ concentration at this depth ($c_{m,ext}^l$) equals the equilibrium CH₄
 1114 concentration $c_{m,eqb}$ at this depth (**Equation C36**):

$$1115 \quad \tilde{c}_m^l(\tilde{L}_z, \tilde{t}) = \tilde{c}_{m,ext}^l = c_{m,eqb}^l(\tilde{L}_z), \quad (\text{C36})$$

1116 where $\tilde{c}_{m,ext}^l$ = normalized specified CH₄ concentration at depth $\tilde{L}_z (= L_z/L_t)$. The
 1117 system, therefore, is charged with CH₄ saturated water at the lowermost boundary.

1118 Similarly, normalized concentrations are specified at \tilde{L}_z for SO₄²⁻ ($\tilde{c}_{s,ext}^l$), DIC
 1119 ($\tilde{c}_{b,ext}^l$) and Ca²⁺ ($\tilde{c}_{ca,ext}^l$). Pore water SO₄²⁻ is consumed above or at the SMT; hence,
 1120 $\tilde{c}_{s,ext}^l$ is zero. Dissolved DIC and Ca²⁺ concentrations are set so they are in equilibrium
 1121 with solubility concentrations of CaCO₃ at depth. Collectively:

$$1122 \quad \tilde{c}_s^l(\tilde{L}_z, \tilde{t}) = \tilde{c}_{s,ext}^l = 0, \quad \tilde{c}_b^l(\tilde{L}_z, \tilde{t}) = \tilde{c}_{b,ext}^l, \quad \tilde{c}_{ca}^l(\tilde{L}_z, \tilde{t}) = \tilde{c}_{ca,ext}^l. \quad (\text{C37})$$

1123 During methanogenesis, a range of solid organic molecules with a range of carbon
 1124 isotope compositions produces CH₄ relatively depleted in ¹³C, and DIC relatively
 1125 enriched in ¹³C. The pathways involved are somewhat complex, especially regarding
 1126 isotope fractionation (**Appendix B**; [Conrad, 2005]). To simplify the modeling, we
 1127 assume a fixed $\delta^{13}\text{C}$ for POC and labile POC ($\delta^{13}\text{C}_{POC}$), and a fixed $\delta^{13}\text{C}$ for CH₄
 1128 generated during methanogenesis ($\delta^{13}\text{C}_{CH_4, meth}$). Both values will be site specific. The
 1129 $\delta^{13}\text{C}_{CH_4, meth}$ values are determined by computing the average values of $\delta^{13}\text{C}$ of CH₄
 1130 [Milkov *et al.*, 2005; Lorenson *et al.*, 2008] measured at the two sites. This implies that
 1131 the fractionation factor (ϵ_m) and the $\delta^{13}\text{C}$ of DIC produced during methanogenesis
 1132 ($\delta^{13}\text{C}_{HCO_3, meth}$) will also be fixed at a given site. For the two sites of immediate interest,
 1133 the values are:

1134 $\delta^{13}C_{POC} = -24\text{‰}$ $\delta^{13}C_{CH_4, meth} = -70\text{‰}$ (Site 1244), (C38)

1135 and

1136 $\delta^{13}C_{POC} = -22\text{‰}$ $\delta^{13}C_{CH_4, meth} = -75\text{‰}$ (Site KC151-3). (C39)

1137 Fractionation factor (ϵ_m) is defined as the ratio of $\delta^{13}C$ of labile POC and CH_4 .

1138
$$\epsilon_m = \frac{\delta^{13}C_{POC} + 1000}{\delta^{13}C_{CH_4} + 1000}$$
 (C40)

1139 The $\delta^{13}C_{HCO_3, meth}$ values and the fractionation factors at these sites are calculated
 1140 using the carbon isotope compositions $\delta^{13}C_{POC}$, and $\delta^{13}C_{CH_4, meth}$.

1141 $\delta^{13}C_{HCO_3, meth} = +22\text{‰}$ $\epsilon_m = 1.049$ (Site 1244), (C41)

1142 and

1143 $\delta^{13}C_{HCO_3, meth} = +31\text{‰}$ $\epsilon_m = 1.057$ (Site KC151-3). (C42)

1144 The carbon isotope composition of DIC ($\delta^{13}C_{HCO_3}$) produced by organoclastic
 1145 sulfate reduction is equated to that of POC ($\delta^{13}C_{POC}$). For sediment at respective sites:

1146 $\delta^{13}C_{HCO_3, POC} = \delta^{13}C_{POC} = -24\text{‰}$ (Site 1244), (C43)

1147 and

1148 $\delta^{13}C_{HCO_3, POC} = \delta^{13}C_{POC} = -22\text{‰}$ (Site KC151-3). (C44)

1149 The $\delta^{13}C$ of CH_4 ($\delta^{13}C_{CH_4}$) and DIC ($\delta^{13}C_{HCO_3}$) at the basal boundary (\tilde{L}_z) are
 1150 specified as observed in field data [Milkov *et al.*, 2005; Torres and Rugh, 2006;
 1151 Lorenson *et al.*, 2008; Kastner *et al.*, 2008a]. For Site 1244:

1152 $\delta^{13}C_{CH_4}(\tilde{L}_z, \tilde{t}) = \delta^{13}C_{CH_4,ext} = -65\text{‰}$, $\delta^{13}C_{HCO_3}(\tilde{L}_z, \tilde{t}) = \delta^{13}C_{HCO_3,ext} = +20\text{‰}$. (C45)

1153 For Site KC151-3:

1154 $\delta^{13}C_{CH_4}(\tilde{L}_z, \tilde{t}) = \delta^{13}C_{CH_4,ext} = -70\text{‰}$, $\delta^{13}C_{HCO_3}(\tilde{L}_z, \tilde{t}) = \delta^{13}C_{HCO_3,ext} = +10\text{‰}$. (C46)

1155

1156 **Acknowledgments**

1157 We acknowledge financial support from the Shell Center for Sustainability, and
1158 the Department of Energy (DE-FC26-06NT42960). We thank the captains, crews and
1159 fellow shipboard scientists of ODP Leg 204 and the GOM JIP for successful drilling and
1160 the collection and analyses of samples. This work was supported in part by the Shared
1161 University Grid at Rice funded by NSF under Grant EIA-0216467, and a partnership
1162 between Rice University, Sun Microsystems, and Sigma Solutions, Inc. We also thank
1163 Editor André Revil, Associate Editor, Walter S. Borowski and an anonymous reviewer
1164 for their constructive and critical commentaries on this manuscript.

1165

1166 **References**

- 1167 Allison, P. A., S. P. Hessebo, and C. E. Brett (2008), Methane seeps on an Early
1168 Jurassic dysoxic seafloor. *Palaeogeography, Palaeoclimatology, Palaeoecology*,
1169 270: 230-238.
1170
- 1171 Archer D., B. A. Buffett, and V. Brovkin (2009), Ocean methane hydrates as a slow
1172 tipping point in the global carbon cycle, *Proc. Natl. Acad. Sci. U.S.A.*, 106, 49,
1173 20596-20601.
1174
- 1175 Berner, R. A. (1980), *Early Diagenesis: A Theoretical Approach*, Princeton Univ. Press,
1176 Princeton, N.J.
1177
- 1178 Bhatnagar, G., W. G. Chapman, G. R. Dickens, B. Dugan, and G. J. Hirasaki (2007),
1179 Generalization of gas hydrate distribution and saturation in marine sediments by
1180 scaling of thermodynamic and transport processes, *Am. J. Sci.*, 307, 861-900.
1181
- 1182 Bhatnagar, G., W. G. Chapman, G. R. Dickens, B. Dugan, and G. J. Hirasaki (2008),
1183 Sulfate-methane transition as a proxy for average methane hydrate saturation in
1184 marine sediments, *Geophys. Res. Lett.*, 35, L03611,
1185 doi:10.1029/2007GL032500.
1186
- 1187 Bhatnagar, G., S. Chatterjee, W. G. Chapman, B. Dugan, G. R. Dickens, and G. J.
1188 Hirasaki (2011), Analytical theory relating the depth of the sulfate-methane
1189 transition to gas hydrate distribution and saturation, *Geochem. Geophys.*
1190 *Geosyst.*, 12, Q03003, doi:10.1029/2010GC003397.
1191
- 1192 Bohrmann, G., J. Greinert, E. Suess, and M.E. Torres (1998), Authigenic carbonates
1193 from the Cascadia subduction zone and their relation to gas hydrate stability,
1194 *Geology*, 26, 647-650.
1195
- 1196 Borowski, W. S., C. K. Paull, and W. Ussler III (1996), Marine pore-water sulfate profiles
1197 indicate *in situ* methane flux from underlying gas hydrate, *Geology*, 24(7), 219
1198 655-658.
1199
- 1200 Borowski, W. S. and C. K. Paull (1997), The gas hydrate detection problem:
1201 Recognition of shallow-subbottom gas hazards in deep-water areas,
1202 *Proceedings, Offshore Tech. Conf.*, vol. 1 OTC-8297, 211-216.
1203
- 1204 Borowski, W. S., C. K. Paull, and W. Ussler III (1999), Global and local variations of
1205 interstitial sulfate gradients in deep-water, continental margin sediments:
1206 Sensitivity to underlying methane and gas hydrates, *Mar. Geol.*, 159, 131–154.
1207
- 1208 Borowski, W. S., N. Cagatay, Y. Ternois, and C. K. Paull (2000), Data report: carbon
1209 isotopic composition of dissolved CO₂, CO₂ gas, and methane, Blake-Bahama
1210 Ridge and northeast Bermuda Rise, ODP Leg 172, *In Keigwin, L.D., Rio, D.,*
1211 *Acton, G.D., and Arnold, E. (Eds.), Proc. ODP, Sci. Results, 172*, College

1212 Station, TX (Ocean Drilling Program), 1–16
1213 doi:10.2973/odp.proc.sr.172.201.2000.
1214
1215 Botz, R., E. Faber, M. J. Whiticar, and J. M. Brooks (1988), Authigenic carbonates in
1216 sediments from the Gulf of Mexico, *Earth Planet. Sci. Lett.*, *88*, 263-272.
1217
1218 Boudreau, B. P., and J. T. Westrich (1984), The dependence of bacterial sulfate
1219 reduction on sulfate concentration in marine sediments, *Geochim. Cosmochim.*
1220 *Acta*, *48*, 2503-2516.
1221
1222 Briaud, J.L., and A. Chaouch (1997), Hydrate melting in soil around hot conductor, *J.*
1223 *Geotech. Geoenviron.*, *123*, 645-653.
1224
1225 Buffett, B. A. and D. Archer (2004), Global inventory of methane clathrate: Sensitivity to
1226 changes in the deep ocean, *Earth Planet. Sci. Lett.*, *227*, 185–199.
1227
1228 Campbell, K. A. (2006), Hydrocarbon seep and hydrothermal vent paleoenvironments
1229 and paleontology: Past developments and future research directions,
1230 *Palaeogeography, Palaeoclimatology, Palaeoecology*, *232*, 362-407.
1231
1232 Castellini, D. G., G. R. Dickens, G. T. Snyder, and C. D. Ruppel (2006), Barium
1233 recycling in shallow sediment above active mud volcanoes in the Gulf of Mexico,
1234 *Chem. Geol.*, *226*, 1-30.
1235
1236 Claypool, G.E., A. V. Milkov, Y. J. Lee, M. E. Torres, W. S. Borowski, and H. Tomaru
1237 (2006), Microbial methane generation and gas transport in shallow sediments of
1238 an accretionary complex, southern Hydrate Ridge (ODP Leg 204), offshore
1239 Oregon, USA, *In Tréhu, A.M., Bohrmann, G., Torres, M.E., and Colwell, F.S.*
1240 *(Eds.), Proc. ODP, Sci. Results, 204: College Station, TX (Ocean Drilling*
1241 *Program), 1–52, doi:10.2973/odp.proc.sr.204.113.2006.*
1242
1243 Collett, T. S. (2002), Energy resource potential of natural gas hydrates. *AAPG Bull.*, *86*,
1244 1971–1992.
1245
1246 Conrad, R. (2005), Quantification of methanogenic pathways using stable carbon
1247 isotopic signatures: a review and a proposal, *Org. Geochem.*, *36*, 739–752.
1248
1249 Cook, A. E., D. Goldberg, and R. L. Kleinberg (2008), Fracture-controlled gas hydrate
1250 systems in the northern Gulf of Mexico, *Mar. Petr. Geol.*, *25*, 932-941.
1251
1252 Daigle, H., and B. Dugan (2010), Origin and evolution of fracture-hosted methane
1253 hydrate deposits, *J. Geophys. Res.*, *115*, B11103, doi:10.1029/2010JB007492.
1254
1255 Davie, M. K. and B. A. Buffett (2001), A numerical model for the formation of gas
1256 hydrate below the seafloor, *J. Geophys. Res.*, *106*, 497-514.
1257

1258 Davie, M. K., and B. A. Buffett (2003a), Sources of methane for marine gas hydrate:
1259 inferences from a comparison of observations and numerical models, *Earth*
1260 *Planet. Sci. Lett.*, 206, 51-63.
1261
1262 Davie, M. K., and B. A. Buffett (2003b), A steady state model for marine hydrate
1263 formation: Constraints on methane supply from pore water sulfate profiles, *J.*
1264 *Geophys. Res.*, 108, 2495, doi:10.1029/2002JB002300.
1265
1266 D'Hondt, S., B. B. Jorgensen, et al. (2004), Distributions of microbial activities in deep
1267 subseafloor sediments, *Science*, 306(5705), 2216-2221.
1268
1269 Dickens, G. R., C. K. Paull, P. Wallace, and the ODP Leg 164 Shipboard Scientific
1270 Party (1997), Direct measurement of in situ methane quantities in a large gas
1271 hydrate reservoir, *Nature*, 385, 426–428.
1272
1273 Dickens, G. R. (2001a), The potential volume of oceanic methane hydrates with variable
1274 external conditions, *Org. Geochem.*, 32, 1179-1193.
1275
1276 Dickens, G. R. (2001b), Sulfate profiles and barium fronts in sediment on the Blake
1277 Ridge: Present and past methane fluxes through a large gas hydrate reservoir.
1278 *Geochim. Cosmochim. Acta*, 65, 529-543.
1279
1280 Dickens, G. R. (2003), Rethinking the global carbon cycle with a large, dynamic and
1281 microbially mediated gas hydrate capacitor, *Earth Planet. Sci. Lett.*, 213, 169-
1282 183.
1283
1284 Dickens, G. R., and G. T. Snyder (2009), Interpreting upward methane flux, *Fire in the*
1285 *Ice, Winter*, 7-10.
1286
1287 Dugan B. (2008), Fluid flow in the Keathley Canyon 151 mini-basin, Northern Gulf of
1288 Mexico, *Mar. Petr. Geol.* 25, 919–923.
1289
1290 Egeberg, P. K., and G. R. Dickens (1999), Thermodynamic and pore water halogen
1291 constraints on gas hydrate distribution at ODP Site 997 (Blake Ridge). *Chem.*
1292 *Geol.*, 153, 53-79.
1293
1294 Formolo, M. J., T. W. Lyons, C. Zhang, C. Kelley, R. Sassen, J. Horita, and D. R. Cole
1295 (2004), Quantifying carbon sources in the formation of authigenic carbonates at
1296 gas hydrate sites in the Gulf of Mexico, *Chemical Geology*, 205, 253-264.
1297
1298 Goni, M. A., K. C. Ruttenberg, and T. I. Eglington (1998), A reassessment of the
1299 sources and importance of land-derived organic matter in surface sediments from
1300 the Gulf of Mexico, *Geochim. Cosmochim. Acta*, 62, 3055–3075.
1301
1302 Greinert, J., G. Bohrmann, and E. Suess (2001), Methane-venting and gas hydrate-
1303 related carbonates at the hydrate ridge: Their classification, distribution and

1304 origin, In C. K. Paull and W. P. Dillon (Eds.), *Natural Gas Hydrates: occurrence,*
1305 *distribution, and detection*, AGU Geophysical Monograph, 124, 99-113.
1306

1307 Hiruta, A., G. T. Snyder, H. Tomaru, and R. Matsumoto (2009), Geochemical
1308 constraints for the formation and dissociation of gas hydrate in an area of high
1309 methane flux, eastern margin of the Japan Sea, *Earth Planet. Sci. Lett.*, 279, 3-4,
1310 326-339.
1311

1312 Iversen, N., and B. B. Jørgensen (1993), Diffusion coefficients of sulfate and methane in
1313 marine sediments: Influence of porosity, *Geochim. Cosmochim. Acta*, 57, 571-
1314 578.
1315

1316 Kastner, M., M. E. Torres, E. Solomon, and A. J. Spivack (2008a), Marine pore fluid
1317 profiles of dissolved sulfate: do they reflect *in situ* methane fluxes? *Fire in the Ice,*
1318 *Summer*, 6-8.
1319

1320 Kastner, M., G. Claypool, and G. Robertson (2008b), Geochemical constraints on the
1321 origin of the pore fluids and gas hydrate distribution at Atwater Valley and
1322 Keathley Canyon, Northern Gulf of Mexico, *Mar. Petr. Geol.* 25, 860-872,
1323 doi:10.1016/j.marpetgeo.2008.01.022.
1324

1325 Kharaka, Y. K., A. S. Maest, W. W. Carothers, L. M. Law, and P. J. Lamothe (1987),
1326 Geochemistry of metal-rich brines from central Mississippi Salt Dome basin,
1327 USA, *Appl. Geochem.*, 2, 543– 561.
1328

1329 Kim, J. H., M. H. Park, U. Tsunogai, T. J. Cheong, B. J. Ryu, Y. J. Lee, H. C. Han, J. H.
1330 Oh, and H. W. Chang (2007), Geochemical characterization of the organic
1331 matter, pore water constituents and shallow methane gas in the eastern part of
1332 the Ulleung Basin, East Sea (Japan Sea), *Island Arc*, 16, 93–104.
1333

1334 Kim, J. H., M. H. Park, J. H. Chun, and Y. J. Lee (2011), Molecular and isotopic
1335 signatures in sediments and gas hydrate of the central/southwestern Ulleung
1336 Basin: high alkalinity escape fuelled by biogenically sourced methane, *Geo-Mar.*
1337 *Lett.*, 31, 37–49, doi: 10.1007/s00367-010-0214-y.
1338

1339 Klauda, J. B., and S. I. Sandler (2005), Global distribution of methane hydrate in ocean
1340 sediment: *Energy and Fuels*, 19, 459–470.
1341

1342 Kvenvolden, K. A. (1993), Gas hydrates: Geological perspective and global change,
1343 *Rev. Geophys.*, 31,173-187.
1344

1345 Kvenvolden, K. A. (1995), A review of the geochemistry of methane in natural gas
1346 hydrate, *Organic Geochem.*, 23, 997-1008.
1347

- 1348 Kwon T. H., K. I. Song, and G. C. Cho (2010), Destabilization of Marine Gas Hydrate-
1349 Bearing Sediments Induced by a Hot Wellbore: A Numerical Approach, *Energy &*
1350 *Fuels*, 24, 5493-5507.
1351
- 1352 Lee, M. W., and T. S. Collett (2006), Gas hydrate and free gas saturations estimated
1353 from velocity logs on Hydrate Ridge, offshore Oregon, U.S.A. In Tréhu, A. M.,
1354 Bohrmann, G., Torres, M.E., and Colwell, F.S. (Eds.), *Proc. ODP, Sci. Results*,
1355 204: College Station, TX (Ocean Drilling Program), 1–25.,
1356 doi:10.2973/odp.proc.sr.204.103.2006.
1357
- 1358 Lee, M. W., T. S. Collett (2008), Integrated analysis of well logs and seismic data to
1359 estimate gas hydrate concentrations at Keathley Canyon, northern Gulf of
1360 Mexico, *Mar. Petr. Geol.*, 25, 924–931.
1361
- 1362 Li, Y., and S. Gregory (1974), Diffusion of ions in sea water and in deep-sea sediments:
1363 *Geochim. Cosmochim. Acta*, 38, 703-714.
1364
- 1365 Liu, X. L. and P. B. Flemings (2007), Dynamic multiphase flow model of hydrate
1366 formation in marine sediments, *J. Geophys. Res.*, 112, B03101, doi:
1367 10.1029/2005JB004227.
1368
- 1369 Lorenson, T. D., G. E. Claypool, and J. A. Dougherty (2008), Natural gas geochemistry
1370 of sediments drilled on the Gulf of Mexico JIP cruise. *Mar. Petr. Geol.*, 25, 873-
1371 883.
1372
- 1373 Lowenstein T. K., M. N. Timofeeff, S. T. Brennan, L. A. Hardie, and R. M. Demicco
1374 (2001), Oscillations in Phanerozoic seawater chemistry: evidence from fluid
1375 inclusions: *Science*, 294, 1086–1088.
1376
- 1377 Luff, R., and K. Wallman (2003), Fluid flow, methane fluxes, carbonate precipitation and
1378 biogeochemical turnover in gas hydrate-bearing sediments at Hydrate Ridge,
1379 Cascadia Margin: Numerical modeling and mass balances, *Geochim.*
1380 *Cosmochim. Acta*, 67, 3403-3421.
1381
- 1382 Macpherson, G. L. (1989), Lithium, boron and barium in formation waters and
1383 sediments, northwestern Gulf of Mexico Sedimentary Basin, *Ph.D. dissertation*,
1384 University of Texas, Austin, Texas, USA.
1385
- 1386 Malinverno, A., M. Kastner, M. E. Torres, and U. G. Wortmann (2008), Gas hydrate
1387 occurrence from pore water chlorinity and downhole logs in a transect across the
1388 Northern Cascadia margin (Integrated Ocean Drilling Program Expedition 311),
1389 *J. Geophys. Res.*, 113, B08103, doi:10.1029/2008JB005702.
1390
- 1391 Milkov, A. V., G. E. Claypool, Y.J. Lee, W. Xu, G. R. Dickens, W. S. Borowski, and ODP
1392 Leg 204 Scientific Party (2003), In situ methane concentrations at Hydrate Ridge,

1393 offshore Oregon: new constraints on the global gas hydrate inventory from an
1394 active margin, *Geology*, 31, 833–836.
1395
1396 Milkov, A. V. (2004), Global estimates of hydrate-bound gas in marine sediments: how
1397 much is really out there? *Earth-Sci. Rev.*, 66, 183-197.
1398
1399 Milkov, A. V., G. R. Dickens, G. E. Claypool, Y. J. Lee, W. S. Borowski, M. E. Torres,
1400 W. Xu, H. Tomaru, A. M. Tréhu, and P. Schultheiss (2004), Co-existence of gas
1401 hydrate, free gas, and brine within the regional gas hydrate stability zone at
1402 Hydrate Ridge (Oregon margin): evidence from prolonged degassing of a
1403 pressurized core, *Earth Planet. Sci. Lett.*, 222, 829-843.
1404
1405 Milkov, A. V. (2005), Molecular and stable isotope compositions of natural gas hydrates:
1406 A revised global dataset and basic interpretations in the context of geological
1407 settings, *Organic Geochem.*, 36(5), 681-702.
1408
1409 Milkov, A. V., G. E. Claypool, Y.J. Lee, and R. Sassen (2005), Gas hydrate systems at
1410 Hydrate Ridge offshore Oregon inferred from molecular and isotopic properties of
1411 gas hydrate-bound and void gases, *Geochim. Cosmochim. Acta*, 69(4), 1007-
1412 1026, doi:10.1016/j.gca.2004.08.021.
1413
1414 Paull, C. K., R. Matsumoto, P. J. Wallace, and W. P. Dillon (1996), *Proc. ODP Init.*
1415 *Repts.*, 164, College Station, TX, (Ocean Drilling Program),
1416 doi:10.2973/odp.proc.ir.164.1996.
1417
1418 Paull, C. K., and R. Matsumoto (2000), Leg 164 overview, *In* Paull, C. K., R.
1419 Matsumoto, P. J. Wallace, and W. P. Dillon, (Eds.), *Proc. ODP, Sci. Results*, 164,
1420 College Station, TX (Ocean Drilling Program), 3–10,
1421 doi:10.2973/odp.proc.sr.163.204.2000.
1422
1423 Paull, C. K., T. D. Lorenson, G. Dickens, W. S. Borowski, W. Ussler III, and K.
1424 Kvenvolden (2000a), Comparisons of *in situ* and core gas measurements in ODP
1425 Leg 164 bore holes, *Annals of the New York Academy of Sciences*, 912, 23-31.
1426
1427 Paull, C. K., T. D. Lorenson, W. S. Borowski, W. Ussler, III, K. Olsen, and N. M.
1428 Rodriguez (2000b), Isotopic composition of CH₄, CO₂ species, and sedimentary
1429 organic matter within samples from the Blake Ridge: gas source implications. *In*
1430 *Paull, C. K., R. Matsumoto, P. J. Wallace, W. P. Dillon, (Eds.), Proc. ODP, Sci.*
1431 *Results*, 164, College Station, TX (Ocean Drilling Program), 67-78,
1432 doi:10.2973/odp.proc.sr.164.207.2000.
1433
1434 Paull, C. K., W. Ussler III, T. Lorenson, W. Winters, and J. Dougherty (2005),
1435 Geochemical constraints on the distribution of gas hydrates in the Gulf of Mexico,
1436 *Geo-Mar. Lett.*, 25, 273-280.
1437

- 1438 Peckmann, J., and V. Thiel (2004), Carbon cycling at ancient methane-seeps, *Chem.*
1439 *Geol.*, 205, 443-467.
1440
- 1441 Pohlman, J., C. Ruppel, D. R. Hutchinson, R. Downer, and R. B. Coffin (2008),
1442 Assessing sulfate reduction and methane cycling in a high salinity pore water
1443 system in the northern Gulf of Mexico, *Mar. Petr. Geol.*, 25, 942–951.
1444
- 1445 Pohlman, J., M. Kaneko, V. B. Heuer, R. B. Coffin, and M. Whiticar (2009), Methane
1446 sources and production in the northern Cascadia margin gas hydrate system,
1447 *Earth Planet. Sci. Lett.*, 287, 504-512.
1448
- 1449 Reeburgh, W. S., (1976) Methane consumption in Cariaco trench waters and
1450 sediments, *Earth Planet. Sci. Lett.*, 28, 337-344.
1451
- 1452 Rempel, A. W. and B. A. Buffett (1997), Formation and accumulation of gas hydrate in
1453 porous media, *J. Geophys. Res.*, 102, 10151-10164.
1454
- 1455 Rodriguez, N. M., C. K. Paull, and W. S. Borowski (2000), Zonation of authigenic
1456 carbonates within gas hydrate-bearing sedimentary sections on the Blake Ridge:
1457 offshore southeastern North America, *In* C. K. Paull, R. Matsumoto, P. J.
1458 Wallace, and W. P. Dillon, (Eds.), *Proc. ODP, Sci. Results*, 164: College Station,
1459 TX (Ocean Drilling Program), 301–312, doi:10.2973/odp.proc.sr.164.227.2000.
1460
- 1461 Ruppel, C., R. Boswell and E. Jones (2008), Scientific results from Gulf of Mexico Gas
1462 Hydrates Joint Industry Project Leg 1 Drilling: Introduction and overview, *Mar.*
1463 *Petr. Geol.*, 25, doi: 10.1016/j.marpetgeo.2008.02.007.
1464
- 1465 Shipboard Scientific Party (1996), Sites 997, *In* C. K. Paull, R. Matsumoto, P. J.
1466 Wallace, et al., *Proc. ODP, Init. Repts.*, 164, College Station, TX (Ocean Drilling
1467 Program), 277–334, doi:10.2973/odp.proc.ir.164.110.1996.
1468
- 1469 Shipboard Scientific Party (2003a), Site 1230, *In* D'Hondt, S.L., Jørgensen, B.B., Miller,
1470 D.J., et al., *Proc. ODP, Init. Repts.*, 201: College Station, TX (Ocean Drilling
1471 Program), 1-107, doi:10.2973/odp.proc.ir.201.111.2003.
1472
- 1473 Shipboard Scientific Party (2003b), Site 1244, *In* Tréhu, A.M, Bohrmann, G., Rack, F.R.,
1474 Torres, M.E., et al., *Proc. ODP, Init. Repts.*, 204: College Station, TX (Ocean
1475 Drilling Program), 1-132, doi:10.2973/odp.proc.ir.204.103.2003.
1476
- 1477 Sloan, E. D. J., and C. Koh (2007), *Clathrate hydrates of natural gases*, 3rd ed. CRC
1478 Press
1479
- 1480 Snyder, G. T., A. Hiruta, R. Matsumoto, G. R. Dickens, H. Tomaru, R. Takeuchi, J.
1481 Komatsubara, Y. Ishida, and H. Yu (2007), Pore water profiles and authigenic
1482 mineralization in shallow marine sediments above the methane-charged system

1483 on Umitaka Spur, Japan Sea, *Deep-Sea Res. II*, 54, 1216-1239,
1484 10.1016/j.dsr2.2007.04.001.
1485
1486 Torres, M. E. and W. D. Rugh (2006), Data report: isotopic characterization of dissolved
1487 inorganic carbon in pore waters, *In Tréhu, A. M., G. Bohrmann, M. E. Torres, and*
1488 *F. S. Colwell, (Eds.), Leg 204, Proc. ODP, Sci. Results, 204*, College Station, TX,
1489 (Ocean Drilling Program) doi:10.2973/odp.proc.sr.204.117.2006.
1490
1491 Torres, M. E. and M. Kastner (2009), Data report: clues about carbon cycling in
1492 methane-bearing sediments using stable isotopes of the dissolved inorganic
1493 carbon, IODP Expedition 311, *In Riedel, M., Collett, T.S., Malone, M.J., and the*
1494 *Expedition 311 Scientists Proc. IODP, 311*, Washington, DC, Integrated Ocean
1495 Drilling Program, doi:10.2204/iodp.proc.311.206.2009.
1496
1497 Tréhu, A. M., G. Bohrmann, F. R. Rack, M. E. Torres et al. (2003), *Proc. ODP Init.*
1498 *Repts., 204*, College Station, TX (Ocean Drilling Program),
1499 doi:10.2973/odp.proc.ir.204.2003.
1500
1501 Tréhu, A. M., P. E. Long, M. E., Torres, G. Bohrmann, F. R. Rack, T. S. Collett, et al.
1502 (2004), Three-dimensional distribution of gas hydrate beneath southern Hydrate
1503 Ridge: Constraints from ODP Leg 204, *Earth Planet. Sci. Lett.*, 222, 845-862.
1504
1505 Valentine, D. L., and W. S. Reeburgh (2000), New perspectives on anaerobic methane
1506 oxidation, *Environmental Microbiology*, 2, 477-484.
1507
1508 Walsh, M. R., S. H. Hancock, S. J. Wilson, S. L. Patil, G. J. Mordis, R. Boswell, T. S.
1509 Collett, C. A. Koh, and E. D. Sloan (2009), Preliminary report on the commercial
1510 viability of gas production from natural gas hydrates, *Energy Economics*, 31, 815-
1511 823.
1512
1513 Winters, W. J., B. Dugan, and T. S. Collett (2008), Physical properties of sediments
1514 from Keathley Canyon and Atwater Valley, JIP Gulf of Mexico Gas Hydrate
1515 Drilling Program, *Mar. Petr. Geol.*, 25, 896-905.
1516
1517 Xu, W. and C. Ruppel (1999), Predicting the occurrence, distribution, and evolution of
1518 methane gas hydrate in porous marine sediments. *J. Geophys. Res.*, 104, 5081-
1519 5096.
1520
1521 Yu, X., J. Li, J. Gong, J. Chen, X. Jin, L. Young-Lee, H. Li, and J. Xu (2006), Stable
1522 carbon and nitrogen isotopic composition of gas hydrate-bearing sediment from
1523 Hydrate Ridge, Cascadia Margin, *Science in China: Series D Earth Sciences*, 49,
1524 872-880.
1525
1526 Zatsepina, O. Y. and B. A. Buffett (1998), Thermodynamic conditions for the stability of
1527 gas hydrate in the seafloor, *J. Geophys. Res.*, 103, 24127–24139.
1528

1529 **Table 1. Model parameters**
 1530

Symbol	Definition (units)	Hydrate Ridge 1244	Keathley Canyon 151-3
L_{sf}	Seafloor depth (m)	^a 890	^b 1322
P_0	Seafloor pressure (MPa)	8.72	12.95
T_0	Seafloor temperature (°C)	^a 3.8	^b 4
dT/dz	Geothermal gradient (°C/m)	^a 0.061	^b 0.038
L_t	Depth to GHSZ (mbsf)	133.4	314.1
L_s	Depth to SMT (mbsf)	9.2	10.4
\dot{S}	Sedimentation rate (cm/kyr)	27	25
$U_{f, sed}$	Fluid flux due to sedimentation (m/s)	2.85×10^{-13}	2.64×10^{-13}
Pe_1	First Peclet number - compaction-driven fluid flow	0.044	0.095
Pe_2	Second Peclet number - external fluid flow	-1, -2, -3	-2, -3, -5
TOC	Total organic carbon (%)	1.27	0.5
β	Normalized organic content at seafloor	3	0.47
$c_{m, eqb}$	CH ₄ solubility at base of the GHSZ	1.701×10^{-3}	2.101×10^{-3}
$c_{s, o}$	Seawater SO ₄ ²⁻ concentration (mM)	28	
$c_{b, o}$	Seawater DIC concentration (mM)	2.4	
$c_{Ca, o}$	Seawater Ca ²⁺ concentration (mM)	10	
D_m	CH ₄ diffusivity (m ² /s)	^c 0.87×10^{-9}	
D_s	SO ₄ ²⁻ diffusivity (m ² /s)	^c 0.56×10^{-9}	
D_b	DIC diffusivity (m ² /s)	^d 0.60×10^{-9}	
D_{ca}	Ca ²⁺ diffusivity (m ² /s)	^d 0.40×10^{-9}	

Da	Damköhler number (methanogenesis)	0.22	
Da_{POC}	Damköhler number (organoclastic sulfate reduction)	1	
Da_{AOM}	Damköhler number (AOM)	10^8	
λ	Rate constant for methanogenesis (s^{-1})	1.07×10^{-13}	1.94×10^{-14}
λ_{POC}	Rate constant for organoclastic sulfate reduction ($m^3/mol \cdot s$)	5.55×10^{-16}	8.10×10^{-17}
λ_{AOM}	Rate constant for AOM ($m^3/mol \cdot s$)	4.60×10^{-8}	6.71×10^{-9}
$N_{t\phi}$	Ratio of L_ϕ to L_t	1	
ρ_{sed}	Sediment density (kg/m^3)	2650	
ρ_w	Water density (kg/m^3)	1000	

1531

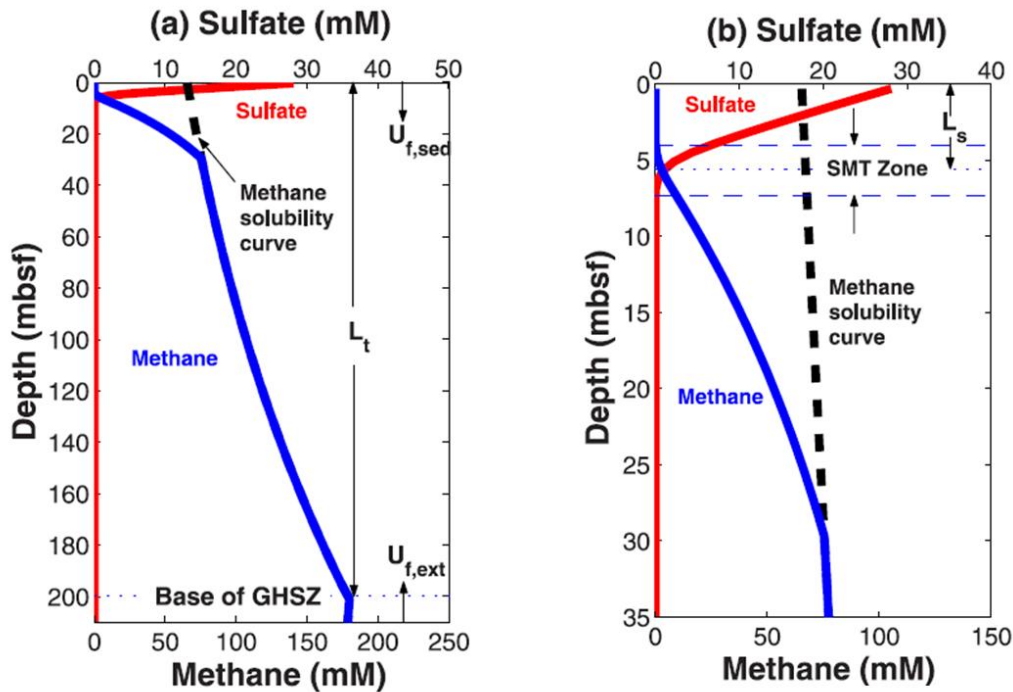
1532 ^a*Tréhu et al.*, [2003]

1533 ^b*Ruppel et al.*, [2008]

1534 ^c*Iversen and Jørgensen*, [1993]

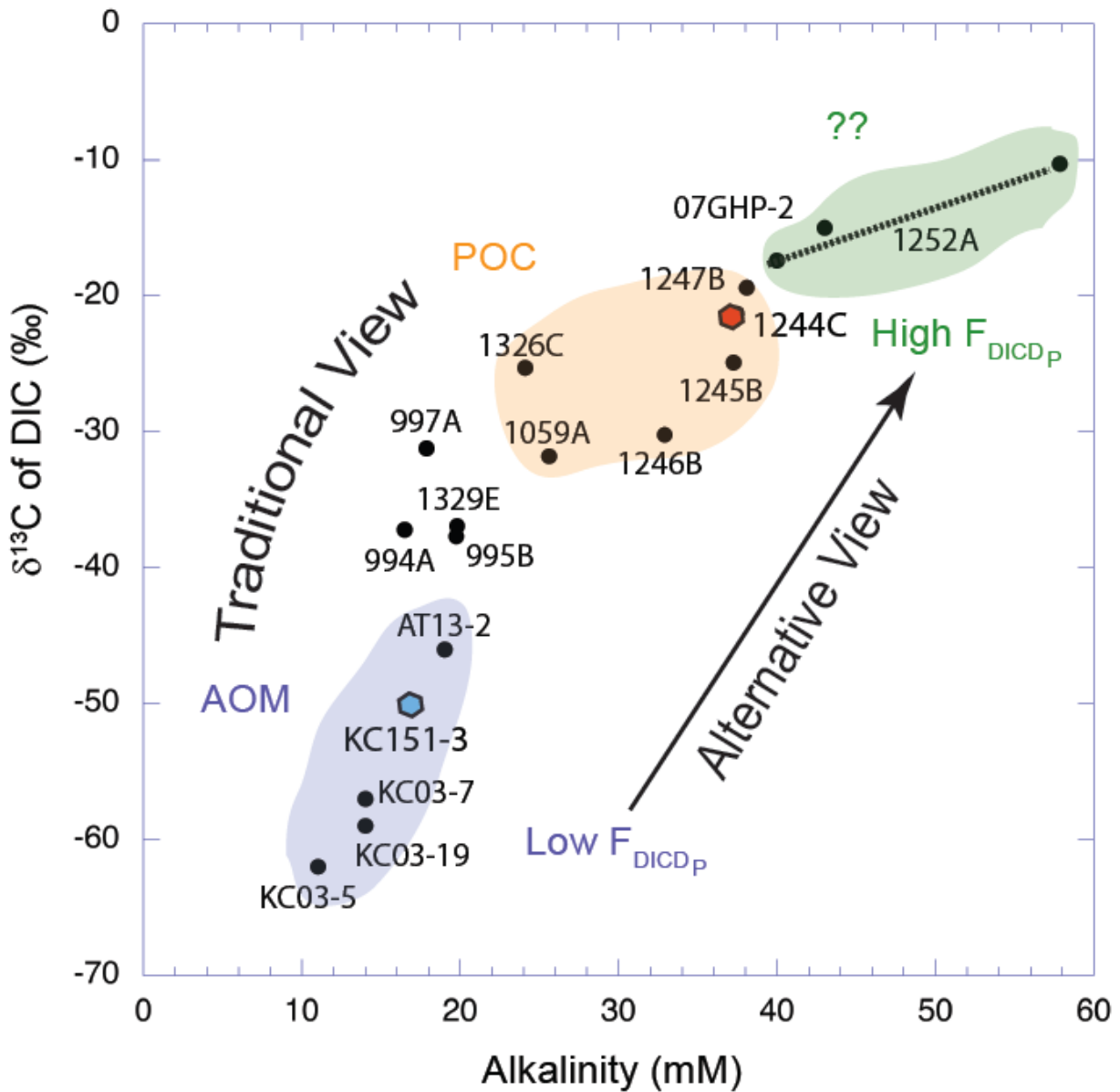
1535 ^d*Li and Gregory*, [1974]

1536



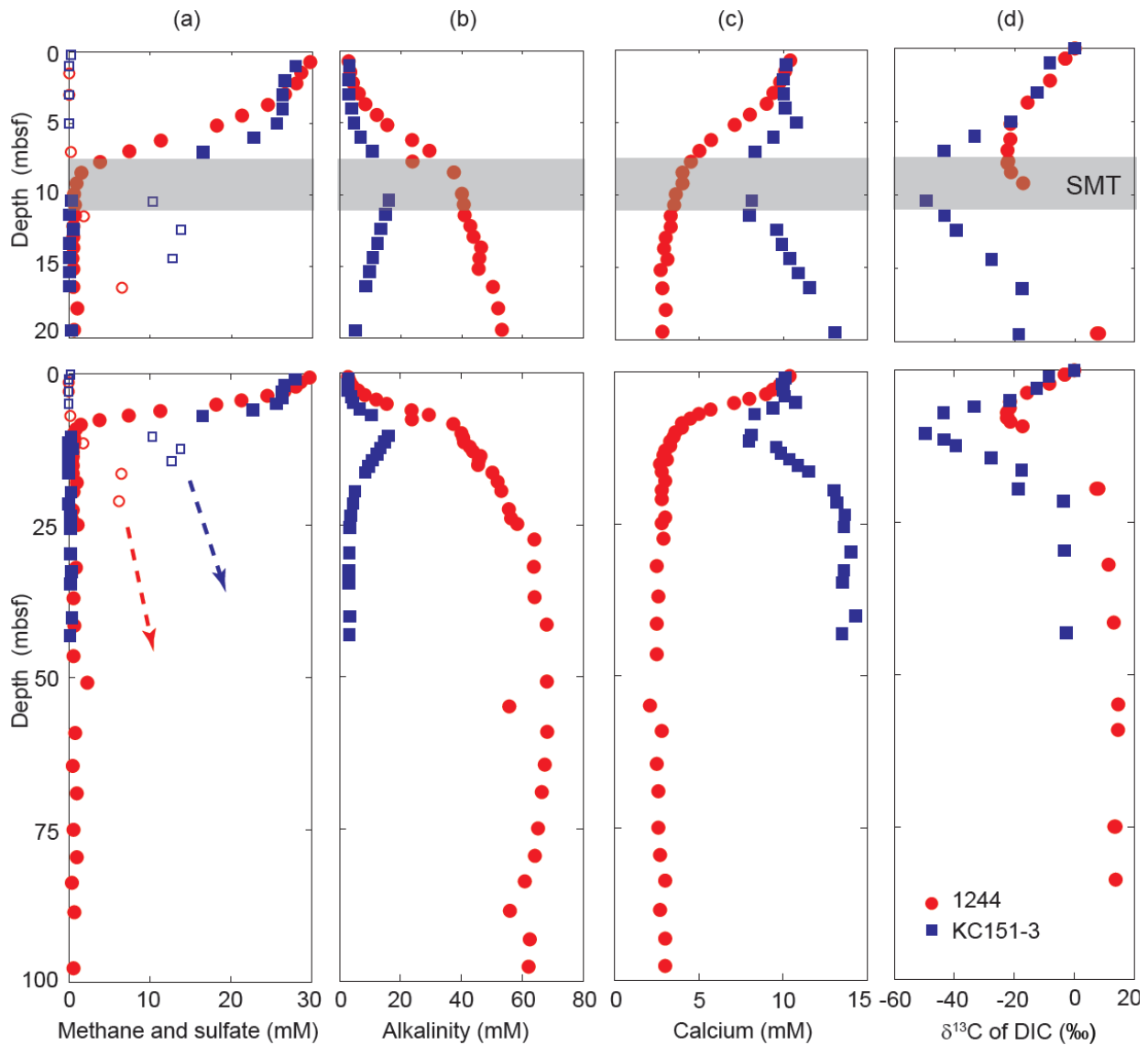
1538

1539 **Figure 1. (a)** Schematic representation of a gas hydrate system showing pore water
 1540 sulfate (red) and methane (blue) concentrations, which go to near zero within the
 1541 sulfate-methane transition (SMT) at shallow depths due to AOM. The dashed line
 1542 represents the methane solubility curve. Fluid fluxes due to compaction-driven flow and
 1543 external flow are denoted as $U_{f, sed}$ and $U_{f, ext}$ respectively; L_t is the depth to the base of
 1544 the gas hydrate stability zone. **(b)** Zoomed sulfate-methane transition (SMT) zone
 1545 showing an overlap of sulfate and methane profiles and its depth below the seafloor
 1546 (L_s) [Bhatnagar *et al.*, 2008]. It should be noted, though, that accurate, high-resolution
 1547 *in situ* CH₄ concentration gradients have never been measured below the SMT [e.g.,
 1548 Dickens *et al.*, 1997; Milkov *et al.*, 2004].
 1549



1550

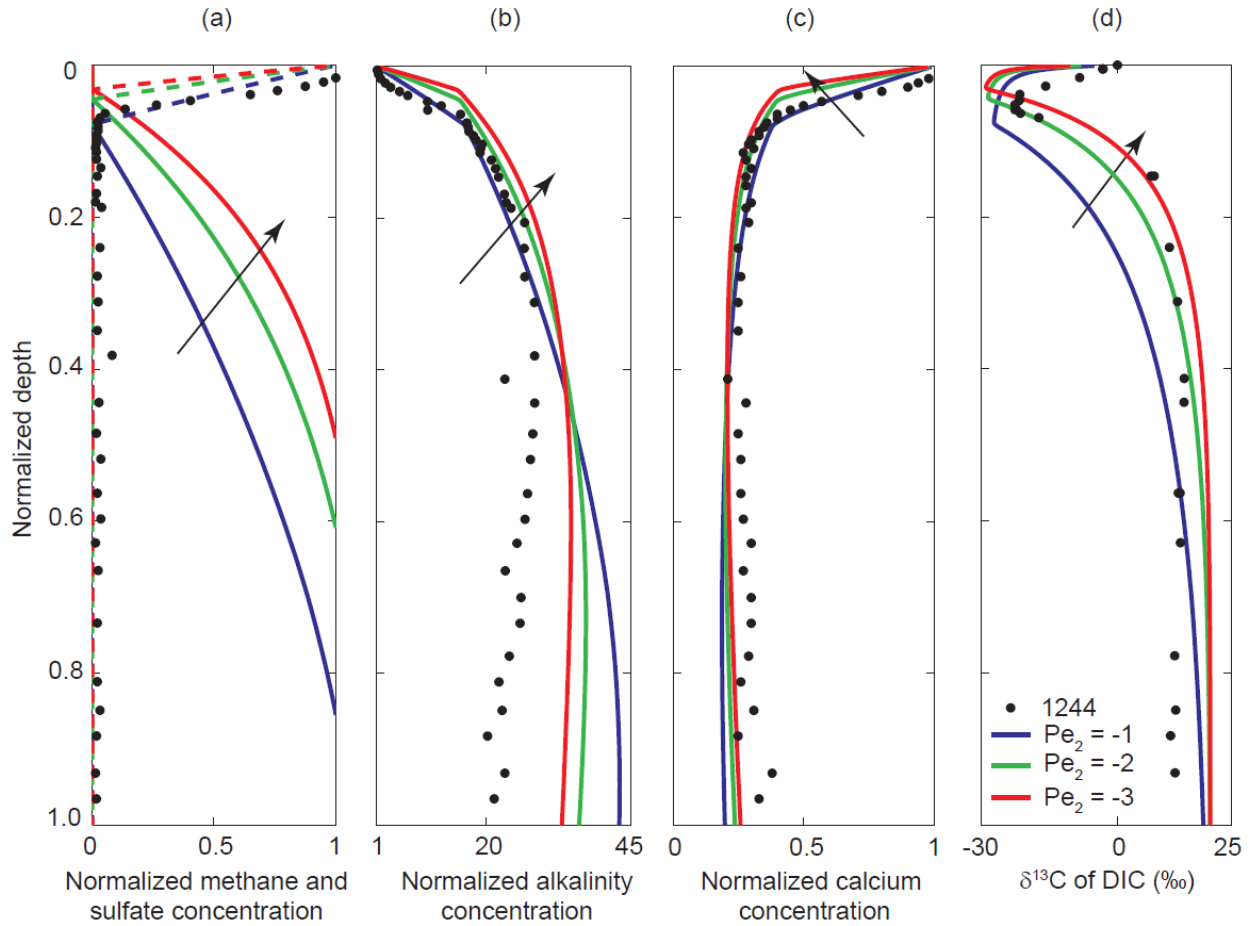
1551 **Figure 2.** Alkalinity versus $\delta^{13}\text{C}$ of DIC at the SMT for multiple locations known to have
 1552 gas hydrate at depth. Note the general trend from sites with low alkalinity and low $\delta^{13}\text{C}$
 1553 of DIC to those with high alkalinity and relatively high $\delta^{13}\text{C}$ of DIC. Traditionally,
 1554 alkalinity and $\delta^{13}\text{C}$ of DIC at the SMT were being used to discriminate between AOM
 1555 and POC-driven sulfate reduction to explain this trend. We suggest the dominant cause
 1556 for this trend arises from the relative flux of upward ^{13}C -enriched DIC (F_{DICDP}). Data
 1557 from: ODP 994-997, *Paull et al.* [2000b]; ODP Site 1059, *Borowski et al.* [2000]; ODP
 1558 Sites 1244-1252, *Claypool et al.* [2006], *Torres and Rugh* [2006]; 1326, 1329, *Torres*
 1559 *and Kastner* [2009]; KC03-5-19, *Pohlman et al.* [2008]; KC151-3-3, AT13-2, *Kastner et*
 1560 *al.* [2008b]; O7GHP-1, *Kim et al.* [2011]. The hatched line for Hole 1252A represents a
 1561 range of values spanning the SMT. Octagons represent the two sites (1244C and
 1562 KC151-3) modeled within this paper.
 1563



1564

1565

1566 **Figure 3.** Pore water (a) SO_4^{2-} (closed circles and squares), CH_4 (open circles and
 1567 squares), (b) alkalinity (DIC), (c) Ca^{2+} concentration and (d) $\delta^{13}\text{C}$ of DIC profiles in
 1568 shallow sediment at Site 1244 in Hydrate Ridge and KC151-3 in Gulf of Mexico. Top
 1569 panel shows the zoomed pore water profiles for the upper 20 m of sediment and the
 1570 shaded region represents the SMT zone. The arrows indicate increasing trend in CH_4
 1571 concentration. Data from: 1244, *Tréhu et al.* [2003] and *Torres and Rugh* [2006];
 1572 KC151-3, *Kastner et al.* [2008b].
 1573



1574

1575

1576

1577

1578

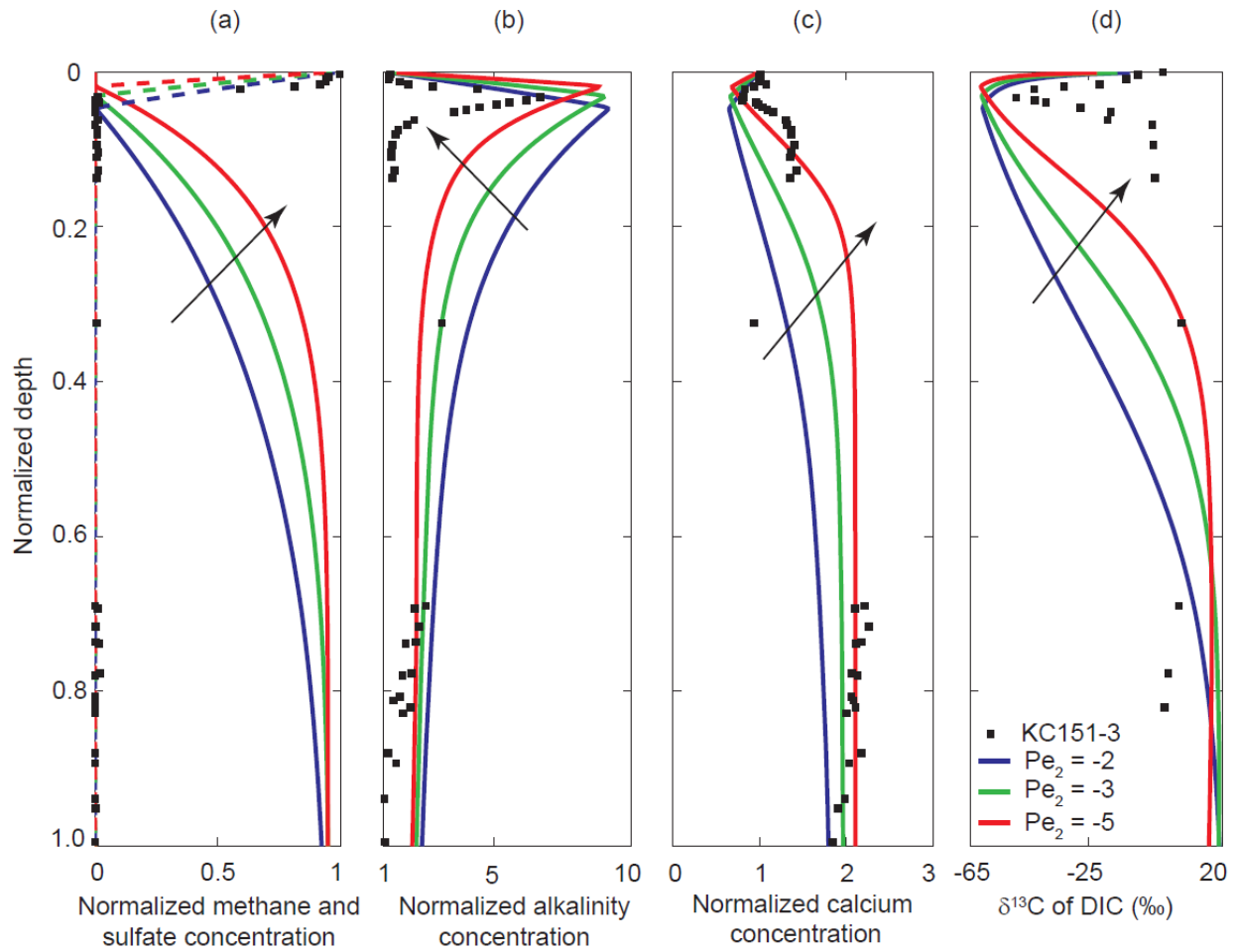
1579

1580

1581

1582

Figure 4. Steady state normalized pore water concentration profiles at Site 1244. (a) CH_4 (solid), and SO_4^{2-} (dashed), (b) DIC, (c) Ca^{2+} , and (d) $\delta^{13}\text{C}$ of DIC. The blue, green and red curves correspond to increasing magnitude of Pe_2 (fluid flux from depth) shown by direction of arrow. Site 1244 data (black circles) [Tréhu *et al.*, 2003; Torres and Rugh, 2006]. Parameters: $\text{Pe}_1 = 0.044$, $\text{Da} = 0.22$, $\text{Da}_{\text{POC}} = 1$, $\text{Da}_{\text{AOM}} = 10^8$, $\beta = 3$, $\tilde{c}_{b,\text{ext}} = 27$ and $\delta^{13}\text{C}_{\text{HCO}_3,\text{ext}} = +20\text{‰}$.

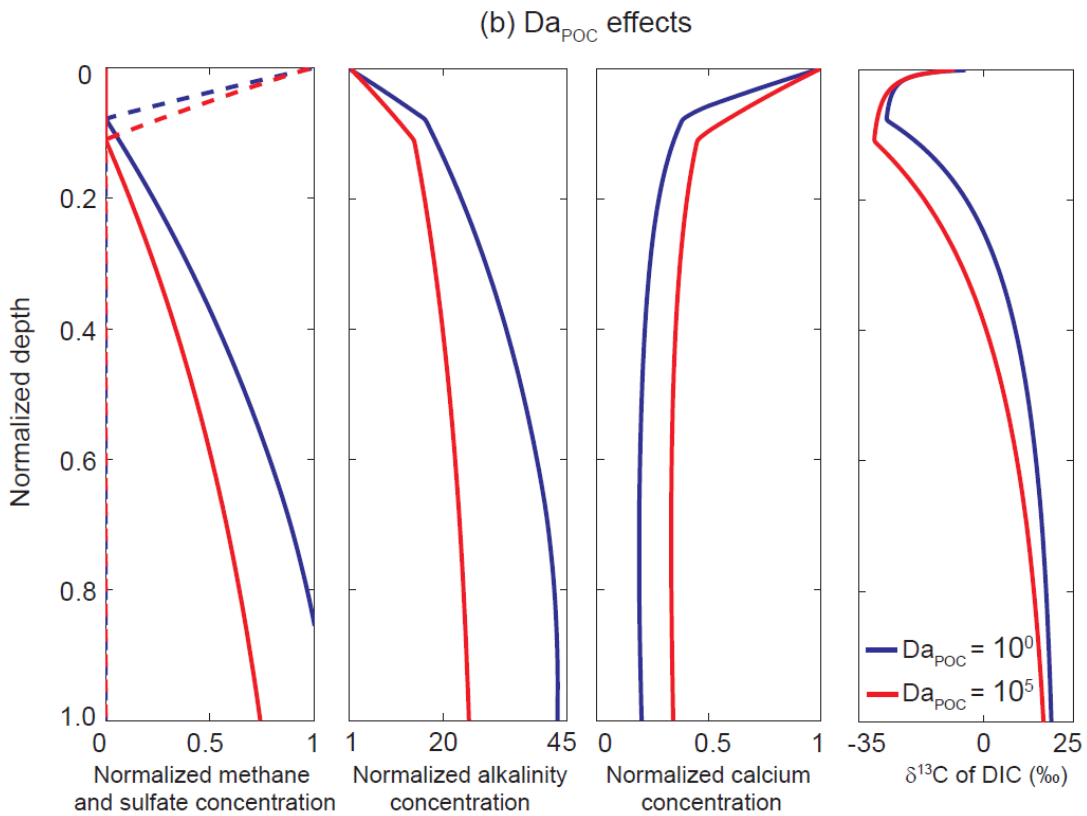
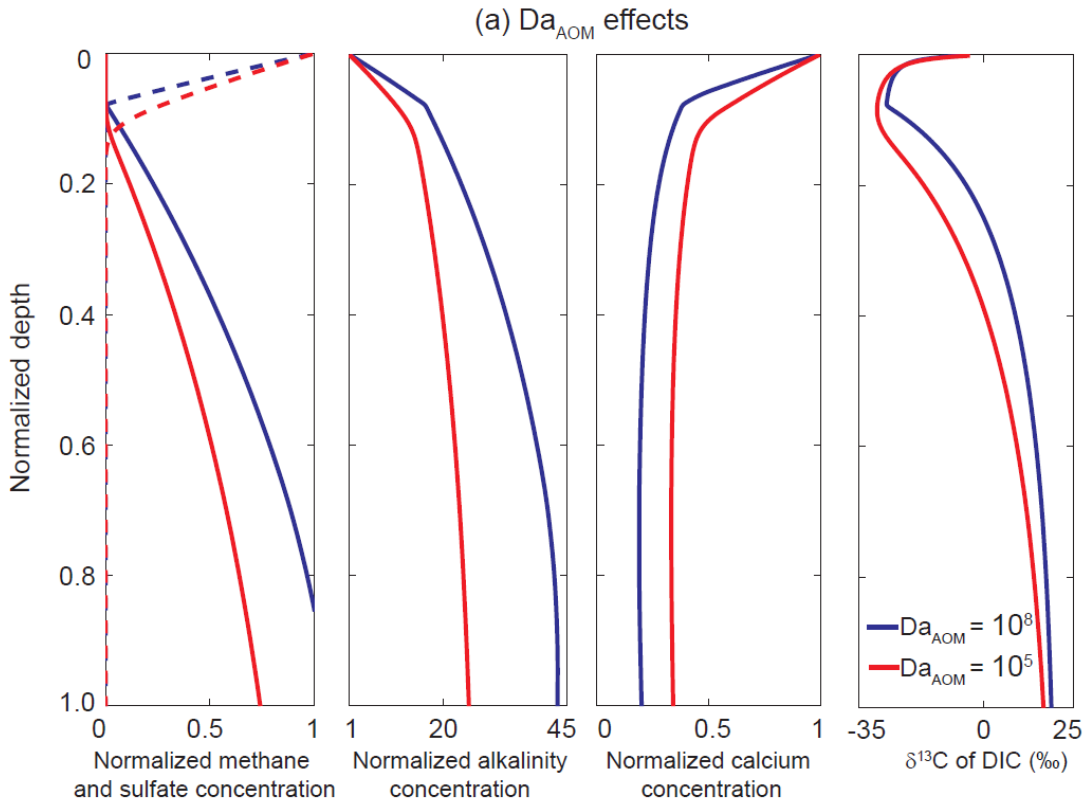


1583
1584

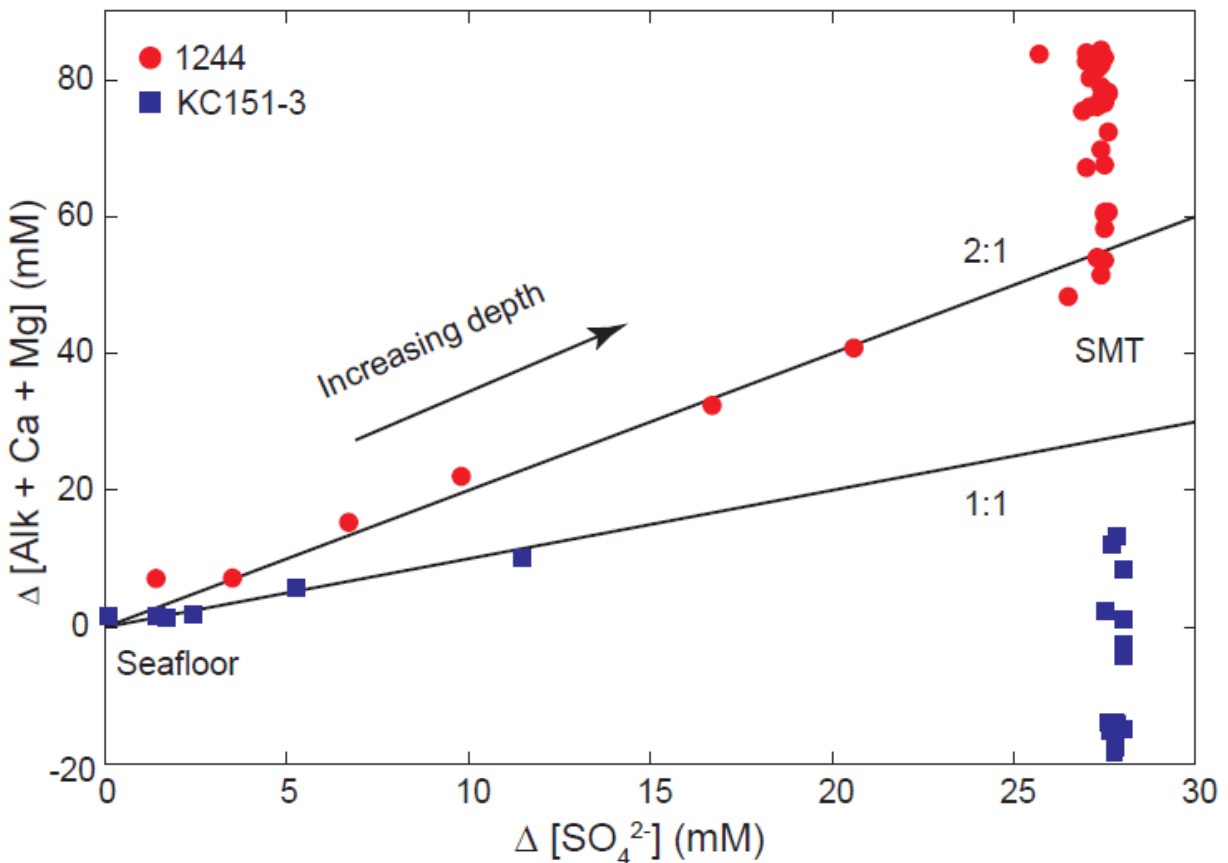
1585 **Figure 5.** Steady state normalized pore water concentration profiles at Site KC151-3.
1586 (a) CH_4 (solid), and SO_4^{2-} (dashed), (b) DIC, (c) Ca^{2+} , and (d) $\delta^{13}\text{C}$ of DIC. The blue,
1587 green and red curves correspond to increasing magnitude of Pe_2 (fluid flux from depth)
1588 shown by direction of arrow. Site KC151-3 data (black circles) [Kastner et al., 2008b].

1589 Parameters: $\text{Pe}_1 = 0.095$, $\text{Da} = 0.22$, $\text{Da}_{\text{POC}} = 1$, $\text{Da}_{\text{AOM}} = 10^8$, $\beta = 0.47$, $\tilde{c}_{b,\text{ext}} = 1.5$ and
1590 $\delta^{13}\text{C}_{\text{HCO}_3,\text{ext}} = +10 \text{‰}$.

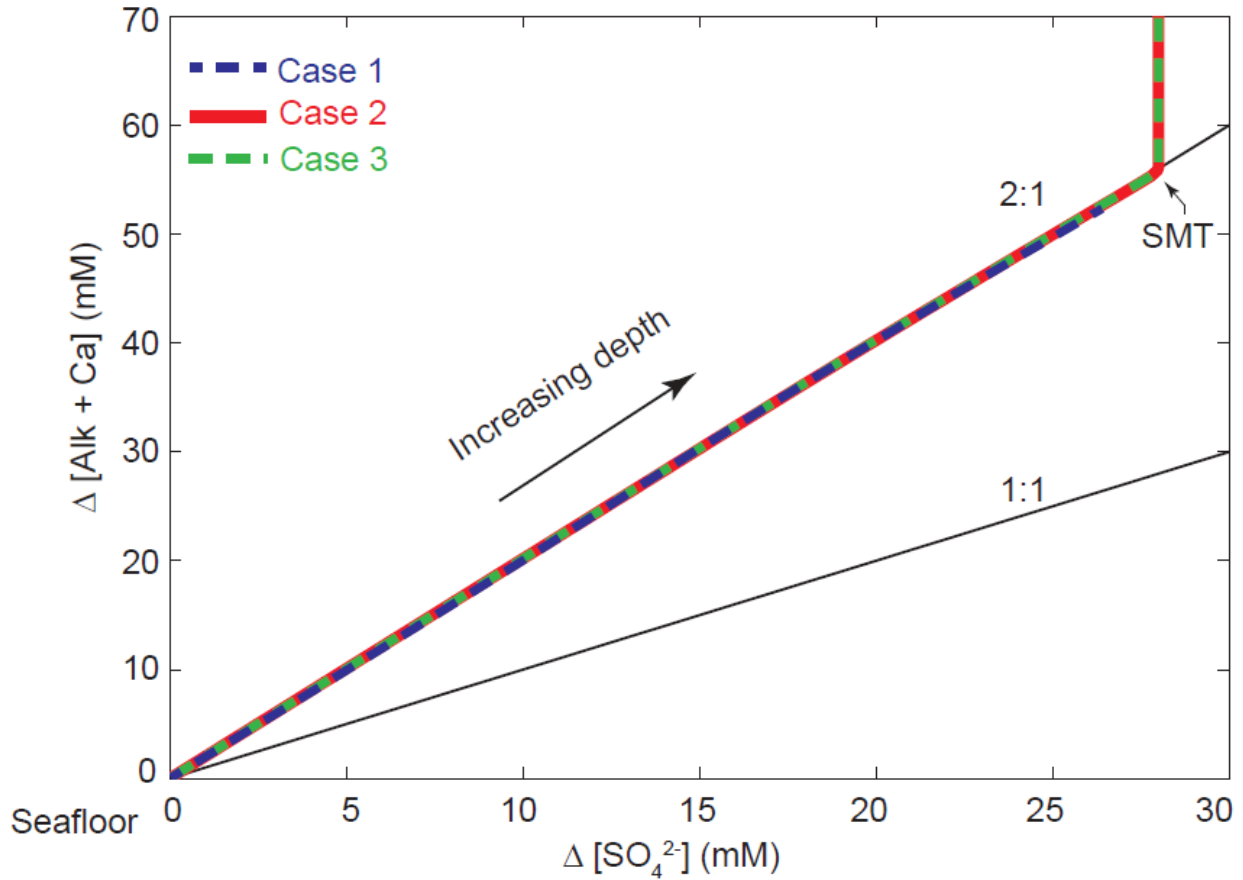
1591
1592



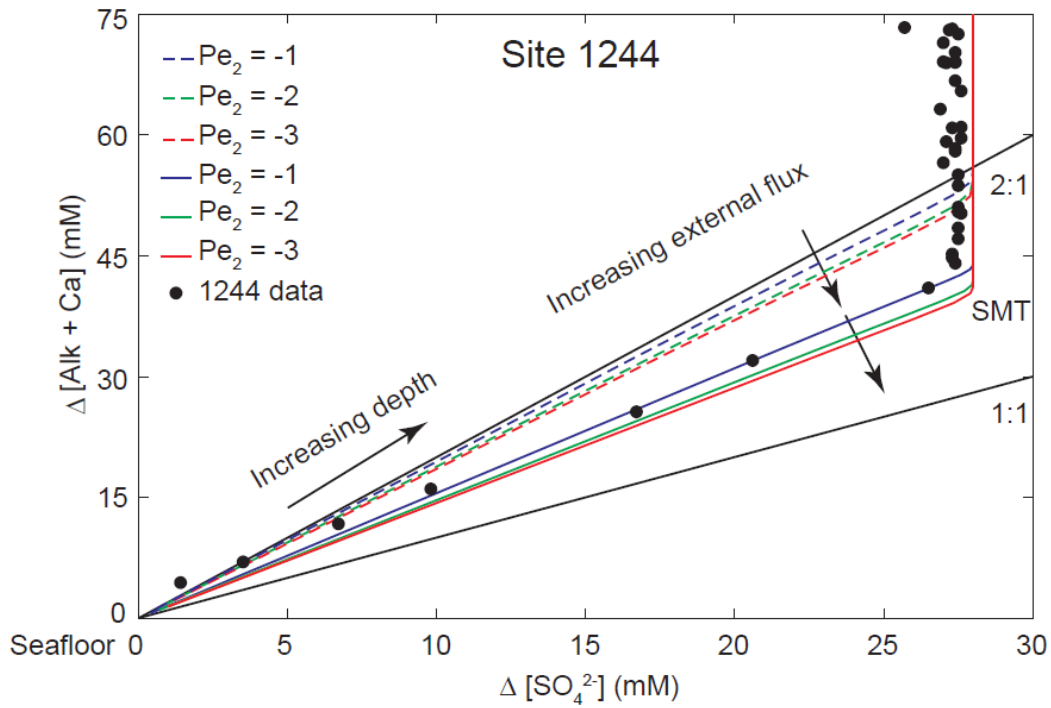
1594 **Figure 6. (a)** Steady state pore water profiles to study the effect of Da_{AOM} at Site 1244.
 1595 Decrease in Da_{AOM} results in a thicker SMT horizon. Parameters: $Pe_1 = 0.044$, $Pe_2 = -1$,
 1596 $Da = 0.22$, $Da_{POC} = 1$, $\beta = 3$, $\tilde{c}_{b,ext} = 27$ and $\delta^{13}C_{HCO_3,ext} = +20$ ‰. **(b)** Effect of Da_{POC} on
 1597 pore water chemistry at Site 1244. Parameters: $Pe_1 = 0.044$, $Pe_2 = -1$, $Da = 0.22$,
 1598 $Da_{AOM} = 10^8$, $\beta = 3$, $\tilde{c}_{b,ext} = 27$ and $\delta^{13}C_{HCO_3,ext} = +20$ ‰. In both cases, decreasing
 1599 Da_{AOM} and increasing Da_{POC} result in higher POC depletion, lesser CH_4 and DIC
 1600 production, greater Ca^{2+} concentration in pore fluids above and below the SMT and a
 1601 more negative $\delta^{13}C$ of DIC at the SMT.
 1602
 1603



1604
 1605
 1606 **Figure 7.** Concentration cross-plot of “excess alkalinity” (ΔAlk^*) corrected for carbonate
 1607 precipitation versus ΔSO_4^{2-} (mM) relative to the seafloor for shallow sediment at Site
 1608 1244 on Hydrate Ridge [Tréhu et al., 2003] and Site KC151-3 [Kastner et al., 2008b].
 1609 As emphasized by Kastner et al. [2008], there is a 2:1 relationship for pore water
 1610 concentrations above the SMT for Site 1244 (red circles) and 1:1 for Site KC151-3 (blue
 1611 squares). Note, however, that excess alkalinity continues to rise below the SMT at Site
 1612 1244. This clearly implies an upward flux of alkalinity from depth; whereas, at Site
 1613 KC151-3, excess alkalinity decrease below the SMT. This decrease is because DIC is
 1614 consumed by Ca^{2+} resulting in calcite precipitation.
 1615

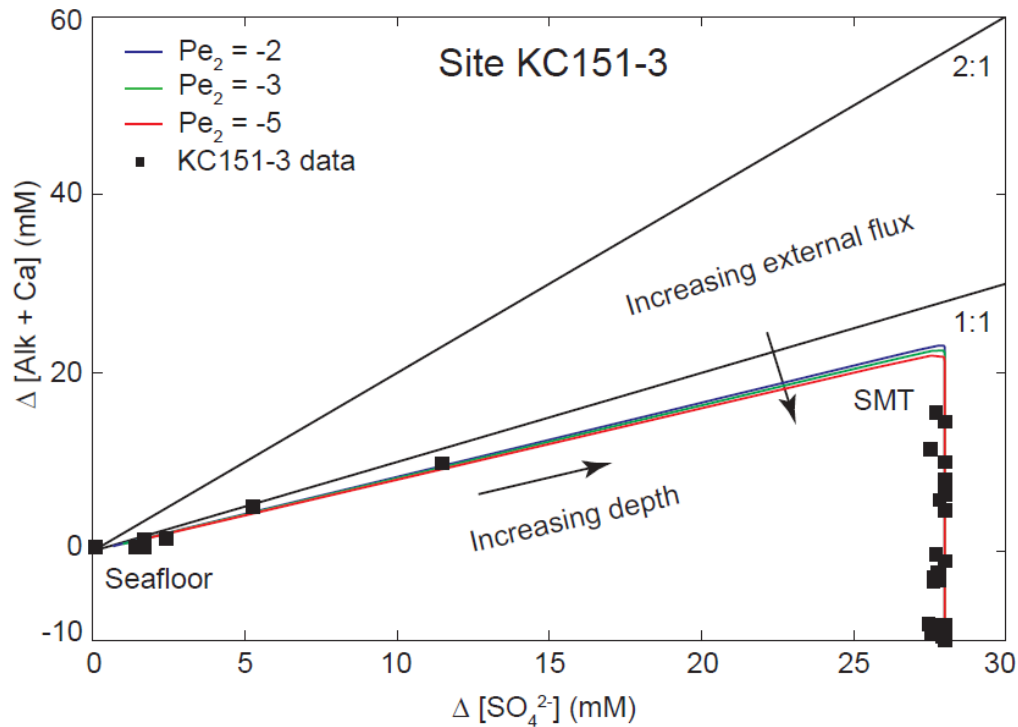


1616
 1617 **Figure 8.** Concentration cross-plots for ΔAlk^* and ΔSO_4^{2-} relative to seawater. Three
 1618 cases are illustrated here corresponding to a 2:1 slope. Blue dashed line represents a
 1619 case with organoclastic sulfate reduction, no upward fluid flux, no AOM and no deep
 1620 DIC source (methanogenesis). Parameters: $Pe_1 = 0.044$, $Pe_2 = 0$, $Da = 0$, $Da_{POC} = 1$,
 1621 $Da_{AOM} = 0$, $\beta = 3$ and $\tilde{c}_{b,ext} = 0$. Red solid line represents another case with low and finite
 1622 upward fluid flux, AOM, methanogenesis, and a deep DIC source, but no organoclastic
 1623 sulfate reduction. Parameters: $Pe_1 = 0.044$, $Pe_2 = -0.1$, $Da = 1$, $Da_{POC} = 0$, $Da_{AOM} = 10^8$,
 1624 $\beta = 3$ and $\tilde{c}_{b,ext} = 79$. The green dashed line represents a third case (combination of the
 1625 first two cases). It is characterized by AOM, organoclastic sulfate reduction,
 1626 methanogenesis, deep DIC source and low upward fluid flux. Parameters: $Pe_1 = 0.044$,
 1627 $Pe_2 = -0.1$, $Da = 1$, $Da_{POC} = 1$, $Da_{AOM} = 10^8$, $\beta = 3$ and $\tilde{c}_{b,ext} = 79$. A 2:1 slope is not only
 1628 achieved by organoclastic sulfate reduction alone, but also by a combined effect of
 1629 AOM, methanogenesis and a deep DIC source. The depth below the seafloor until the
 1630 SMT is shown by the direction of the arrow; below the SMT, ΔAlk^* increases with no
 1631 change in ΔSO_4^{2-} implying high DIC flux entering the SMT from below.
 1632



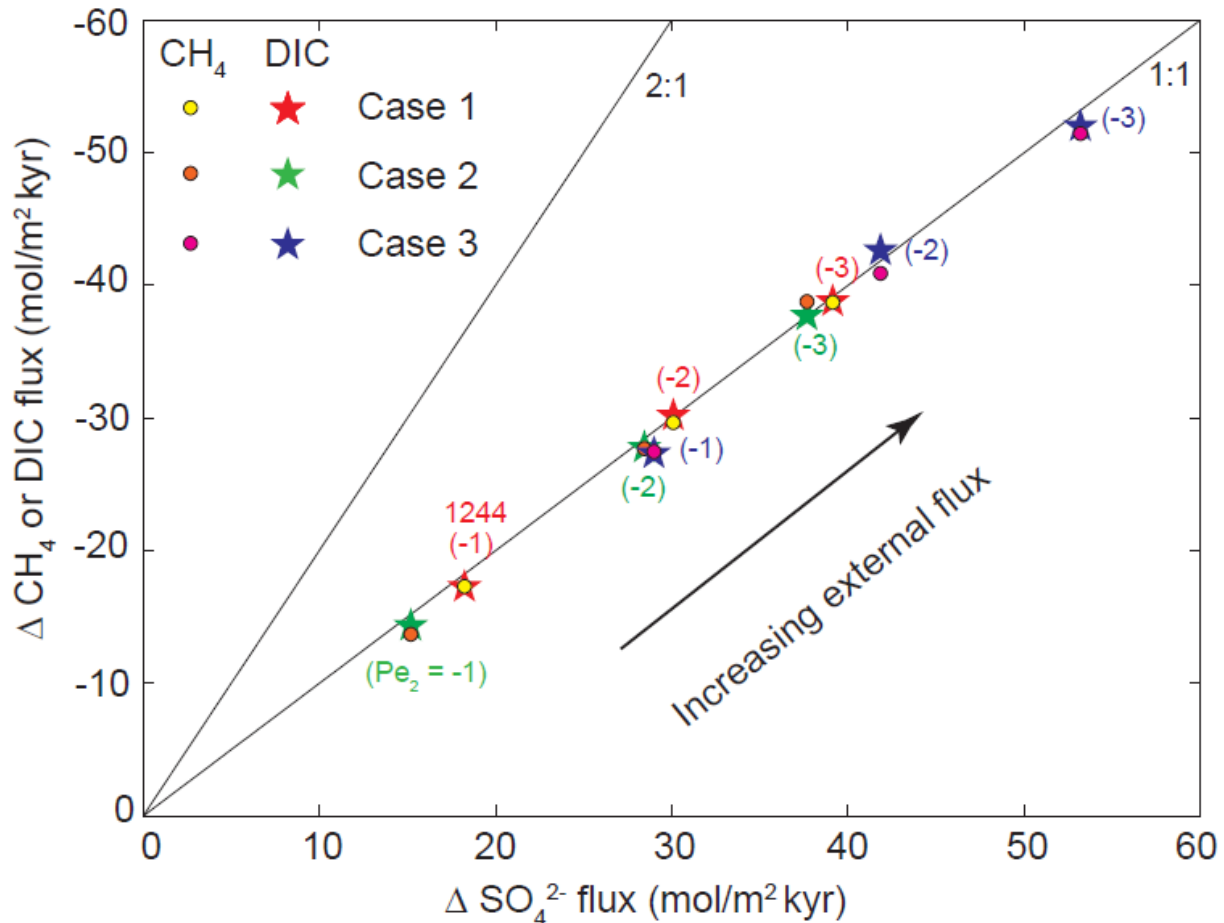
1633
1634

1635 **Figure 9(a).** Concentration cross-plots for ΔAlk^* and ΔSO_4^{2-} relative to the seafloor with
 1636 AOM, organoclastic sulfate reduction, methanogenesis, deep DIC source and upward
 1637 fluid flux at Site 1244. The solid lines correspond to parameters same as in **Figure 4**.
 1638 Dashed lines correspond to a case with higher rate of methanogenesis rate and greater
 1639 DIC flux from depth ($Da=1$ and $\tilde{c}_{b,ext}=50$). The blue, green, and red colors indicate
 1640 increasing fluid flux (corresponding to $Pe_2 = -1, -2$ and -3). Cross-plot constructed from
 1641 Site 1244 data (black circles) [Tréhu et al., 2003] matches well with our simulated cross-
 1642 plots. The slope decreases with increase in fluid flux from depth. Higher DIC input (due
 1643 to higher methanogenesis and/or high DIC source at depth) results in a greater slope.
 1644 Notably, negligence of Mg^{2+} in ΔAlk^* calculations above, results in a slope less than 2:1
 1645 as compared to **Figure 7**.
 1646



1647
 1648
 1649
 1650
 1651
 1652
 1653
 1654
 1655
 1656
 1657
 1658
 1659

Figure 9(b). Concentration cross-plots for ΔAlk^* and ΔSO_4^{2-} relative to the seafloor with AOM, organoclastic sulfate reduction, methanogenesis, relatively depleted DIC source at depth and upward fluid flux at Site KC151-3. Parameters used are same as in **Figure 5**. Increasing upward fluid flux (corresponding to $Pe_2 = -2, -3$ and -5) are represented by blue, green and red curves. Data from Site KC151-3 data [Kastner *et al.*, 2008b] is used to construct cross-plots shown by black circles. The slope of the cross-plot decreases as fluid flux increases (same as in **Figure 9a**). Contrary to **Figure 9a**, ΔAlk^* decreases with no change in ΔSO_4^{2-} beyond the SMT, implying DIC flux leaving the SMT both above and below.



1660
1661

1662 **Figure 10.** Flux cross-plots of CH₄ (circles) and DIC (stars) versus SO₄²⁻ across the
1663 SMT corresponds to a 1:1 slope. Case 1 corresponds to simulations shown in **Figure 4**.
1664 The simulation results that best matches Site 1244 data ($Pe_2 = -1$; **Figure 4**) show 17
1665 mol/m²kyr of SO₄²⁻ entering the SMT from above, 17 mol/m²kyr is the difference
1666 between amounts of DIC entering from below and leaving toward the seafloor (including
1667 carbonate precipitation). This gives a net change of 17 mol/m²kyr of DIC across the
1668 SMT, which balances the downward flux of SO₄²⁻ and supports a 1:1 stoichiometry and
1669 dominance of AOM at the SMT. Case 2 increases the rate of organoclastic sulfate
1670 reduction by two orders of magnitude ($Da_{POC} = 10^2$; all other parameters are same as
1671 Case 1) and the relative flux correspondence across the SMT is unaltered. Case 3
1672 corresponds to high DIC flux entering the SMT from below and high methanogenesis
1673 rate also results in the same 1:1 correlation between CH₄ and DIC fluxes relative to
1674 SO₄²⁻ flux (parameters same as dashed curves in **Figure 9a**). The Pe_2 values
1675 (equivalent to upward fluid flux) are noted in parenthesis and the arrow indicates
1676 increase in upward fluid flux.